

RESEARCH ARTICLE

Multiview tiling light sheet microscopy for 3D high-resolution live imaging

Mostafa Aakhte* and Hans-Arno J. Müller*

ABSTRACT

Light-sheet or selective plane illumination microscopy (SPIM) is ideally suited for *in toto* imaging of living specimens at high temporal-spatial resolution. In SPIM, the light scattering that occurs during imaging of opaque specimens brings about limitations in terms of resolution and the imaging field of view. To ameliorate this shortcoming, the illumination beam can be engineered into a highly confined light sheet over a large field of view and multi-view imaging can be performed by applying multiple lenses combined with mechanical rotation of the sample. Here, we present a Multiview tiling SPIM (MT-SPIM) that combines the Multi-view SPIM (M-SPIM) with a confined, multi-tiled light sheet. The MT-SPIM provides high-resolution, robust and rotation-free imaging of living specimens. We applied the MT-SPIM to image nuclei and Myosin II from the cellular to subcellular spatial scale in early *Drosophila* embryogenesis. We show that the MT-SPIM improves the axial-resolution relative to the conventional M-SPIM by a factor of two. We further demonstrate that this axial resolution enhancement improves the automated segmentation of Myosin II distribution and of nuclear volumes and shapes.

KEY WORDS: Microscopy, Light sheet microscopy, Selective plane illumination microscopy, *Drosophila*, Early development, Gastrulation

INTRODUCTION

The early development of multicellular animals features dramatic tissue movements resulting in the spatial organization of the body plan. An important mechanism driving these dynamic cell and tissue movements are force-producing molecular interactions and their mechanobiological responses (Ladoux and Mège, 2017). In an ideal scenario, the molecular dynamics underlying cell and tissue movements should be investigated in the context of the entire embryo, because all cells are mechanically coupled to some extent. To achieve this goal, robust and fast microscopy methods are required to dynamically image entire developmental processes. The prevailing method for most of these studies in embryogenesis has been confocal-based fluorescence microscopy, because of its high spatial resolution in three-dimensional multi-channel imaging. These applications have provided important information on the biophysics of actomyosin dependent dynamics related to tissue tension and other

mechanical feedback within a tissue (Miao and Blankenship, 2020). However, confocal microscopy of whole embryos is limited by a rather small field of view and the relatively high level of irradiation during the scanning process bearing the risk of phototoxicity. Therefore, it still remains a challenge to image all morphogenetic movements in an embryonic phase such as gastrulation simultaneously and at a subcellular level of optical resolution.

One method that is specifically well suited to address the challenges in dynamic imaging of whole embryos is selective plane illumination microscopy (SPIM). SPIM bypasses some of the limitations of the conventional epifluorescence confocal microscopy (Huisken et al., 2004). The major advancement of the SPIM in comparison with epifluorescence microscopy lies in its ability to image with minimal out-of-focus light and low phototoxicity. These improved imaging parameters are achieved by applying a thin sheet of light to illuminate the sample. The simplest platform of the SPIM, also introduced as the OPEN-SPIM platform, consists of two separate optical arms: The illumination arm and the detection arm, which are arranged at an angle of 90° to each other (Huisken et al., 2004; Pitrone et al., 2013). The illumination arm produces a sheet of light that illuminates only one plane within the sample, a method also known as optical sectioning. The performance of the optical sectioning of a given light sheet is defined by its thickness and its effective range. The effective range of the light sheet determines the imaging field of view (FOV) and these parameters have an inverse relationship with each other (Engelbrecht and Stelzer, 2006): a thick light sheet has a long effective range, but provides poor optical sectioning; a thinner light sheet provides better optical sectioning, but results in a smaller FOV. The ideal set-up should take these parameters into account and will apply a thin light sheet over a large FOV (Fig. S1).

The performance of SPIM is not only limited by the properties of the light sheet itself, but also by the optical properties of a biological sample causing light scattering. When applying wavelengths typically used for fluorescent imaging, the light sheet does not penetrate more than several tens of micrometers into the living biological sample (Fahrbach et al., 2010). This is particularly true for fairly large and opaque specimens, in which the light sheet is heavily diffracted over the imaging FOV, resulting in only a small fraction of the returning well-resolved information (Huisken et al., 2004). Multiview imaging represents one efficient approach to compensate for poor optical sectioning and sample transparency (Krzic et al., 2012; Pitrone et al., 2013). The specimen is rotated mechanically in order to illuminate and image the sample from different angles. The speed of the mechanical rotation is limited to avoid a drift of the sample, resulting in a blurred or de-positioned image. As a consequence, the slow speed rotation creates a time delay between the different views during 3D image capturing. This time delay is particularly crucial when imaging rapidly occurring dynamic events. Moreover, if the mounting of the sample is not centered to the axis of rotation, it creates an additional lateral or axial

Developmental Genetics Group, Institute of Biology, University of Kassel, Heinrich-Plett Strasse 40, 34132 Kassel, Germany.

*Authors for correspondence (aakhte.mostafa@uni-kassel.de; h.a.muller@uni-kassel.de)

DOI: 10.1242/dev.199725; M.A., 0000-0003-4685-5576; H.-A.J.M., 0000-0002-7525-6874

Handling Editor: Thomas Lecuit

Received 18 April 2021; Accepted 13 August 2021

shift during imaging for each rotated view. These limitations can be addressed by re-arranging the basic Multiview imaging to a system with four optical arms consisting of two illumination arms and two detection arms (Krzic et al., 2012; Tomer et al., 2012). The illumination arms create two light sheets that excite the sample from opposite sides and each light sheet covers half of the sample. The emitted light from each FOV is collected by two objective lenses that are arranged orthogonally to the light sheets. Compared with the basic Multiview imaging setup, the Multiview SPIM with four objective lenses is at least four times faster and it provides fewer blurring effects during imaging, thus improving reconstruction and quantification of the imaging data.

Another key factor related to the FOV in Multiview SPIM is the axial resolution of the microscope. Similar to the basic SPIM configuration, the axial resolution of the Multiview SPIM can also be defined by convolution of the light sheet and the point spread function of the detection lens. Two principal approaches can improve the axial resolution of a Multiview SPIM: light sheet engineering and sample rotation. The generation and application of beam engineering to produce the thin light sheet has benefited from using non-structured and structured beams such as Gaussian beam (Keller et al., 2008), Bessel beam (Fahrbach et al., 2010; Gao et al., 2014; Planchon et al., 2011), Airy beam (Nylk et al., 2016; Vettenburg et al., 2014; Yang et al., 2014), Lattice beam (Chen et al., 2014) and more-photon excitations (Truong et al., 2011). Among these structured beams, the conventional Gaussian beam is still the most commonly used excitation form, because it provides the best contrast and light confinement over its effective FOV (Remacha et al., 2020). As described above, the rotation allows for covering the entire 3D FOV within the SPIM setup. In the case of the resolution enhancement with a rotation approach, the four-lenses Multiview SPIM also can be combined with the sample rotation technique such that each quarter of the sample is imaged at least two times from two orthogonal views. This sequential imaging of the sample causes a time delay between two views of each part that may result in a misaligned image fusion when live imaging of subcellular activity is concerned (Tomer et al., 2012). Previous studies have shown that these limitations can be addressed by a complicated Multiview SPIM arrangement in a way that each optical arm functions as illumination and detection at the same time (Chhetri et al., 2015). This helps to increase the accuracy of the imaging process; however, it requires an expensive and large optical setup with four cameras and eight scanning mirrors.

The lack of axial resolution of a light sheet over a large FOV can also be compensated for using the so-called tiling technique, which involves manually moving the sample through the thin light sheet or sweeping multiple thin light sheets inside a large sample (Chmielewski et al., 2015; Dean et al., 2015; Dean and Fiolka, 2014; Gao, 2015). The light-sheet tiling method has the advantage over moving the sample, because it is faster and contact free. The tiled light sheet can be generated by rapidly adjusting the wave-front of the excitation beam using several beam shaping approaches: an electrically tunable lens (Chmielewski et al., 2015), a tunable acoustic index gradient lens (Dean et al., 2015; Gao, 2015), mechanical remote focusing by a piezo electric element (Dean and Fiolka, 2014) or a fast spatial light modulator (SLM) (Fu et al., 2016). Among these methods, the SLM is the most practical beam shaper, because it offers a versatile application for beam shaping, as well as beam aberration correction and beam aperture control simultaneously with the tiling technique (Aakhte et al., 2018). All of these approaches were successfully applied to the basic configuration of the SPIM with two or three objective lenses

(Chakraborty et al., 2019; Chen et al., 2020; Dean et al., 2015; Dean and Fiolka, 2014; Fu et al., 2016; Gao, 2015; Tsai et al., 2020; Voigt et al., 2019; Wang et al., 2019) to imaging a small transparent specimen or cleared fixed sample, but are not optimized for high-resolution whole functional imaging of an opaque live sample.

In the present work, we combined the simultaneous M-SPIM with the tiling light sheet technique to create a novel robust SPIM for high-resolution live imaging. In our technique, a large and opaque specimen like the *Drosophila* embryo can be imaged from four different views with high spatio-temporal resolution without any rotation. First, we demonstrate the concept of MT-SPIM based on the implication of a fast SLM to tile the scanning light sheet. The broad versatility of MT-SPIM is demonstrated by live imaging of MyoII-GFP in early *Drosophila* embryos. We compared the axial resolution of the recorded data from the tiling MT-SPIM mode with data obtained by the conventional, non-tiling M-SPIM mode. The MT-SPIM technique yields images with a high spatial resolution in 3D over time, which can be employed to reconstruct the natural shape of each cell in a fairly large multicellular organism. We show that 3D imaging with MT-SPIM of the cell nuclei greatly improves automatic segmentation and analysis of nuclei number and volume. We analyzed the imaging data to correlate the dynamics of subcellular MyoII distribution with supracellular MyoII structures within the context of the entire embryo. This analysis revealed the temporal sequence of dynamic MyoII-GFP localization in distinct morphogenetic movements during gastrulation in the *Drosophila* embryo.

RESULTS AND DISCUSSION

Design of the MT-SPIM microscope set-up

The conventional multi-view light sheet microscopy with four objective lenses is based on simultaneous or sequential light sheets to illuminate the sample from two sides (Krzic et al., 2012; Tomer et al., 2012) (Fig. 1A). The dimensions of these two light sheets are usually determined by the size of the sample; thus, ideally each light sheet should cover half of the sample. The standard and commonly used parameter to define the FOV of a light sheet is twice the Rayleigh length, which is the distance from the smallest waist of the light sheet to the point where it becomes 1.4 times wider than its center. Therefore, an inherent feature of the light sheet is a non-uniform axial resolution that results in differences of the imaging quality over the FOV (Fig. S1). For example, a light sheet based on a Gaussian beam needs to cover a 90 μm FOV, when imaging half of the diameter of a *Drosophila* embryo. Accordingly, the waist of this light sheet is about $\sim 2.7 \mu\text{m}$ within the central area, but it becomes $\sim 3.8 \mu\text{m}$ at the edges, causing a loss in axial resolution. To achieve higher levels of resolution, the waist of the light sheet should be even thinner, which, on the other hand, aggravates the compromised optical sectioning at the edges (Fig. S1A,B). In order to overcome this inhomogeneity in optical sectioning, we combined the M-SPIM with a beam tiling method based on a SLM (Fig. 1B).

The optical design of our MT-SPIM set-up is based on a classic arrangement with four objective lenses, where the sample can be dipped into water in the space between the lenses within a sample chamber (Fig. 1C). The sample and illumination objective lenses are in a fixed position and are not moving, which protects the imaging from adverse effects through unwanted movement. The optical illumination paths include a fast SLM and two scanning mirrors: a Y-Galvo mirror and a Z-Galvo mirror. The Y-Galvo mirror scans the illumination beam along the height of the imaging FOV (y -axis) to generate the light sheet, and the Z-Galvo mirror scans the light sheet through the sample for volume imaging. At the same time, the SLM

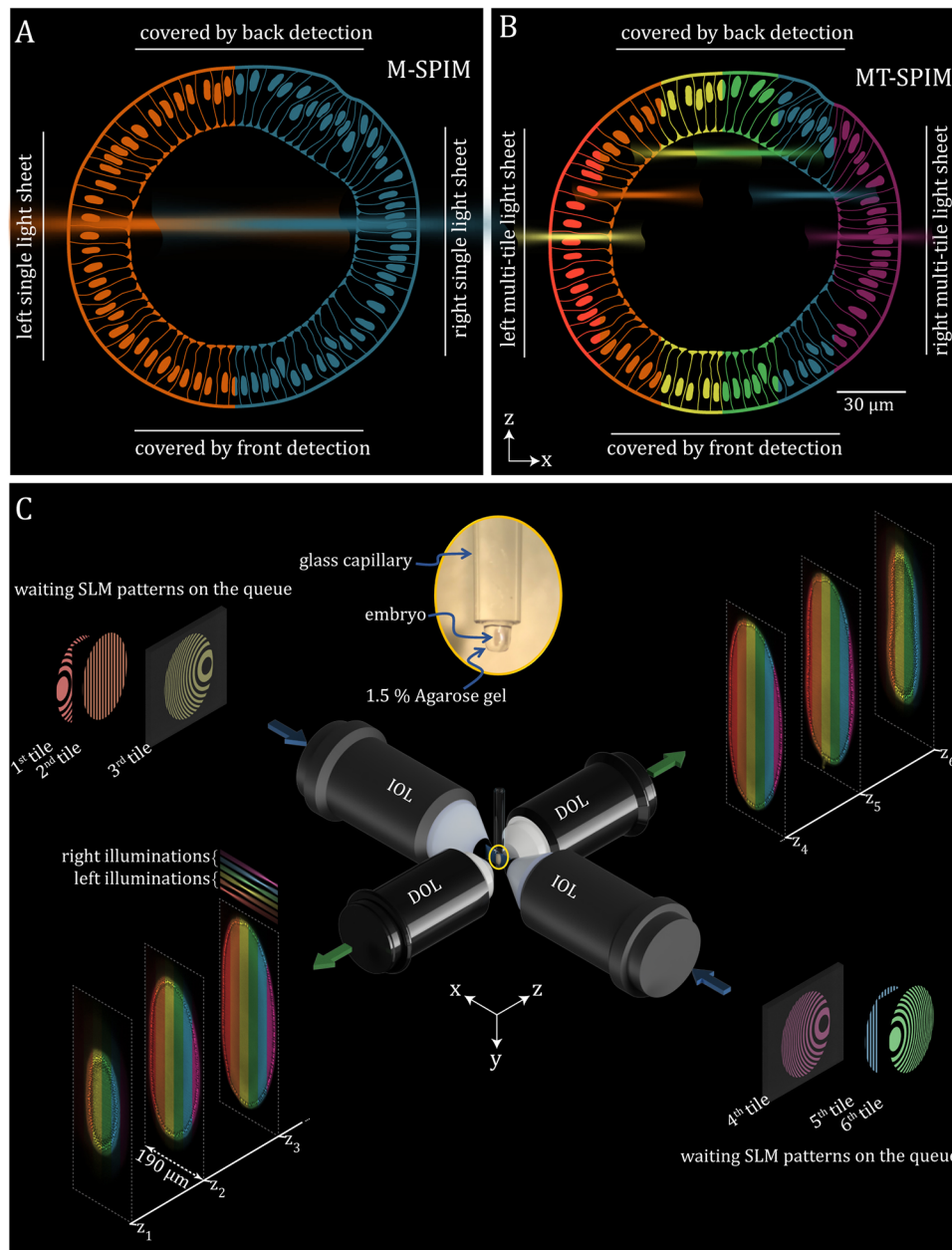


Fig. 1. The principle of Multiview tiling selective plane illumination microscopy. (A) Concept of the conventional Multiview selective plane illumination microscopy (M-SPIM) from the axial view (xz plane). The sample is illuminated with two homogeneous and thick light sheets from opposite directions, which are color-coded with blue and orange. (B) Design of Multiview tiling selective plane illumination microscopy (MT-SPIM) with six tiles of illumination in which each tile covers 16.6% of the volume. (C) The workflow of the MT-SPIM, which consists of four objective lenses; two illumination and two detection lenses. The illumination arms include a spatial light modulator with the combination of two Galvo mirrors (GMy and GMz) to tile, generate and swipe the light sheet in three dimensions through the sample, which is dipped into the water between four objective lenses.

modulates the illumination beam several times per each imaging plane by applying virtual lenses to tile the light sheet in a remote fashion through the x-axis (Fig. 1C; Fig. S2). Each illuminated tile of the sample is recorded independently by rapidly changing the pattern of the SLM, which has a 41 μs time gap between two tiled light sheets. This enables us to rapidly swipe the light sheets over the FOV for near simultaneous illumination. The combination of this illumination technique within a Multiview-SPIM configuration provides the basis for the application of a thin light sheet over the entire *Drosophila* embryo. The temporal resolution of the MT-SPIM supports the time-lapse recording of most morphogenetic movements in 3D.

Enhancing resolution by MT-SPIM imaging

The MT-SPIM setup provides improved dynamic imaging properties by combining a high spatial and temporal resolution. To investigate the properties of the MT-SPIM microscope, we

performed a set of experiments by imaging 2-hour-old, living *Drosophila* embryos expressing Sqh::eGFP [regulatory light chain of non-muscle Myosin II (MyoII) fused to eGFP]. The early *Drosophila* embryo is a large, diffractive sample that requires a $190 \times 190 \times 500 \mu\text{m}^3$ volume FOV for imaging. In order to compare the performance of the MT-SPIM in comparison to the conventional M-SPIM mode, we took advantage of the fast SLM in our system to apply two distinct types of light sheets during imaging in a pseudo-simultaneous fashion. This way, the imaging data using the MT-SPIM mode versus the M-SPIM mode can be assessed much better than comparing results obtained from two different microscopes with distinct specifications. Both light sheets were based on a scanning Gaussian beam: the conventional light sheet waist was uniform along the FOV (around 90 μm) and its full width at half maximum (FWHM) was about 3.2 μm. For the tiling light sheet, we used a Gaussian light sheet with a FWHM on its waist of about 2.2 μm which has a 65 μm effective length (two times of Rayleigh

range) where each single tiling light sheet is non-uniform and its Rayleigh range covers less than half of the embryo (Fig. S3). This means that its waist in the center ($2.2\ \mu\text{m}$) is smaller than at the edges ($3\ \mu\text{m}$), which creates better light confinement and axial resolution in the center of the FOV than at the edges. To compensate the resolution and contrast on the FOV's edges, we have tiled the light sheet several times per illumination arm. For example, to deliver a homogeneous light sheet over the embryo, we have tiled the light sheet three times for each illumination arm (Fig. S4). The center of each tile has $30\ \mu\text{m}$ displacement (one Rayleigh range) from the next tile, which creates a sufficient amount of overlap between the tiled light sheets to generate a homogeneously illuminated area in the MT-SPIM configuration (Fig. S5).

One advantage of the SLM-based Multiview design is to rapidly switch between tiling and non-tiling modes. Thus, a sample can be imaged with different beam engineering techniques simultaneously, which allows a side-by-side comparison of data with M-SPIM and MT-SPIM from the same embryo (Fig. 2A). To examine the

resolution of a microscope in the axial direction (z -axis), the 3D recorded images were reconstructed as maximum intensity projections in the corresponding axial direction (Fig. 2B). The side-by-side comparison of various cellular structures of the Sqh::eGFP embryo in different regions of interest (ROI) illustrates the improved resolution of the dynamic MyoII-GFP localization (Fig. 2C). The Fourier analyses confirm that the frequency components of the MT-SPIM image are more expanded in the z -axis compared with the M-SPIM image; we calculated a twofold improvement of the z -resolution in the tiling mode when compared with the M-SPIM mode (Fig. 2D, Movies 1 and 2). The improvement in axial resolution is crucial for the dynamic visualization of subcellular components in three dimensions. For example, transversal cross-sections of embryos can reveal morphogenetic events in the internal of the *Drosophila* embryo to analyze the localization of MyoII-GFP from dorsal, ventral and lateral views of the embryo at the same time (Fig. 2E). The 3D-rendered data (Fig. 2) show that the MT-SPIM mode improves the

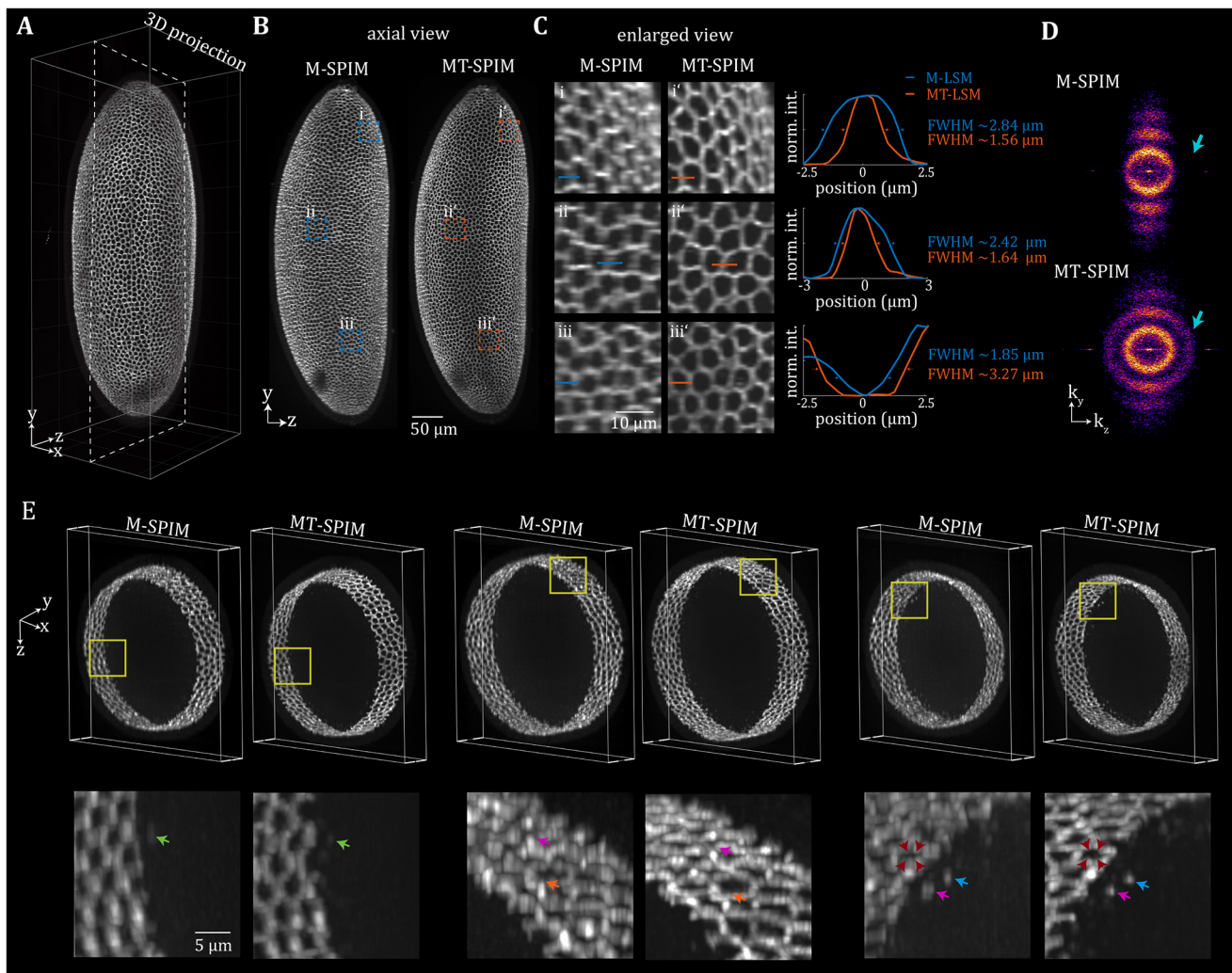


Fig. 2. Improvement of three-dimensional image resolution with MT-SPIM microscopy. (A) 3D rendered image of the whole *Drosophila* embryo expressing Sqh-GFP (non-muscle Myosin II tagged with GFP). (B) Axial view (yz plane) maximum intensity projection of the embryo from the conventional M-SPIM and MT-SPIM. (C) Side-by-side comparison of the of enlarged three regions of interest from images in B. (D) Calculated frequency domain of the images in B, which illustrates the higher spatial frequency in z -direction from the MT-SPIM imaging compared with the conventional M-SPIM. (E) The 3D rendering of the *Drosophila* embryo from its small cross-section from three different 3D ROIs. The arrows in D and E highlight the differences between MT-SPIM and M-SPIM when reconstructing the MyoII accumulation and its natural shape. Red arrowheads indicate the area in between cortical MyoII. Representative data from multiple independent experiments ($n=3$) are shown.

reconstruction accuracy of subcellular details. The subcellular MyoII network is visible at higher resolution not only at the embryo surface but also when the actomyosin network moves into the interior of the embryo during cell formation (Fig. 2E). The MyoII localization around each cell during this rapidly advancing dynamic process can be recovered more precisely by MT-SPIM (Fig. 2E).

Live imaging of early morphogenesis stage in *Drosophila* embryos using MT-SPIM

The MT-SPIM is designed for high-resolution 3D imaging of fairly large specimens over time. The lateral and axial resolutions of the MT-SPIM are measured at $0.74 \pm 0.05 \mu\text{m}$ and $1.55 \pm 0.14 \mu\text{m}$ with deconvolution, respectively (Fig. S6). The imaging speed for the whole embryo volume is 40 s to capture 1300 image frames where the exposure time is set to 20 ms. To explore the full potential of our MT-SPIM method for live imaging, we investigated the dynamic MyoII-GFP distribution during early development. As a proof of principle, we acquired 3D image sequences of 2 h-old live *Drosophila* embryos expressing Sqh::eGFP every 90 s (80 s for simultaneous imaging of tiling and conventional modes and 10 s interval time) for 90 min during cellularization and the beginning of gastrulation (Fig. 3). During this early developmental stage, actomyosin forms a polygonal network over the entire embryo, which moves towards the center of the embryo (Schejter and Wieschaus, 1993). During this inward movement, the actomyosin network changes its configuration, starting with a priming phase to a hexagonal phase and finally ending in a ring phase where individual actomyosin rings contract (Krueger et al., 2019).

The lateral (*xy* plane) and axial views (*yz* plane) of the sample were reconstructed for each time point by fusing the tiles using content-based image fusion (Fig. 3A,B). The improved optical sectioning capability and the removal of out-of-focus signals are apparent in the MT-SPIM images in the lateral and in the axial direction (Fig. 3A,B; Movie 3). A side-by-side comparison of the reconstructed data indicated artifacts in the M-SPIM data concerning the distribution of MyoII-GFP during the different phases of cell formation. MyoII-GFP was lacking or strongly reduced at several anterior-posterior cell boundaries, suggesting a partially planar polarized distribution at the onset of cellularization (Fig. 3Ci-v). During the priming phase of cellularization, a temporary, uneven MyoII-GFP distribution is based upon a gradual increase in MyoII-GFP intensities at the newly forming furrows (He et al., 2016). In the M-SPIM mode, the MyoII-GFP localization suggested a partially planar polarized distribution (Fig. 3Ci-v). In contrast, the MT-SPIM mode can resolve a larger range of MyoII-GFP intensities during the formation of new cell boundaries at the entry of cellularization. The comparison of the two modes at this stage of development illustrates how a poor resolution in SPIM can mislead the interpretation of a dynamic subcellular distribution of GFP-tagged proteins.

When comparing the average distance between two opposite bicellular contacts at an identical position, it became apparent that the MT-SPIM resolution is improved as the distance appears $1 \mu\text{m}$ shorter when compared with M-SPIM (Fig. 3Di-v). This difference can become even more extreme when the network enters the ring phase, where the individual rings cannot be resolved in M-SPIM mode, but can be imaged as discrete structures in MT-SPIM imaging (Fig. 3Cv,D). The MT-SPIM microscope also greatly improved the resolution when imaging various subcellular and supracellular MyoII-GFP structures that form during gastrulation movements (Fig. 3E). We conclude that the increased axial

resolution of the MT-SPIM is crucial to provide an improved reconstruction of subcellular MyoII-GFP structures within the context of the entire development of the early *Drosophila* embryo.

4D dynamic imaging of MyoII-GFP distribution during selected morphogenetic movements in the *Drosophila* gastrula

The MT-SPIM imaging provides an excellent method to study the dynamic changes in the distribution of GFP-tagged proteins in the context of early *Drosophila* embryogenesis. A whole range of different morphogenetic movements have been well studied during gastrulation and the actomyosin cytoskeleton was shown to be involved in most of these events (Gheisari et al., 2020). The simultaneous imaging of MyoII-GFP in the embryo at the mesoscale has provided important information about the relationship of mechanical forces in instructing cell flows during gastrulation movements in *Drosophila* (Streichan et al., 2018). Although individual subcellular and supracellular MyoII structures have been detailed by high-resolution confocal microscopy, these structures have not been imaged in the context of the entire early embryo, including internal tissues. We therefore applied the MT-SPIM to dynamically image the distribution of MyoII-GFP and quantified fluorescence intensities in selected events during gastrulation (Fig. 4, Movie 4).

During cellularization, the polygonal actomyosin network moves from the periphery of the embryo towards the center. Towards the end of cell formation, the maximum depth of the network varies along the periphery of the embryo; we measured a depth of about $42 \pm 0.1 \mu\text{m}$ in the middle section and $24 \pm 0.25 \mu\text{m}$ at the poles (Fig. 4C,D). We quantified the MyoII-GFP intensities for three well-described morphogenetic movements during gastrulation: ventral furrow formation, cephalic furrow formation and posterior midgut formation (Fig. 4B). During ventral furrow formation, MyoII-GFP intensities at the apical domains of the presumptive mesoderm cells arise at about 30 min after the start of cellularization and gradually increase during early gastrulation. Synchronously, the MyoII-GFP intensities at the cephalic furrow begin to increase, but to a much slower extent compared with the ventral domain. At the posterior pole the first fluctuations in MyoII-GFP intensities were observed before the onset of gastrulation, which were caused by the mitotic activities of the pole cells (Fig. 4E,E'). A strong MyoII-GFP intensity increase is observed in the posterior midgut invagination with 7.5 min delay after the highest peak of MyoII-GFP in the presumptive ventral furrow. These data show that the first changes in MyoII-GFP occur in the ventral domain followed by the cephalic furrow and last in the posterior midgut primordium.

The data also allowed us to calculate the rate changes of MyoII-GFP intensities for the individual morphogenetic movements (Fig. 4E). We found that MyoII-GFP rate changes followed a different pattern between the different morphogenetic events. In the cephalic furrow, the increase in MyoII-GFP levels occurred without any notable rate changes. In contrast, the increase in the ventral furrow showed alternating phases of high and low rates of intensity changes. The posterior midgut exhibited also alternating rate changes; however, with a longer amplitude than the ventral furrow. These results indicate that rate changes underlying the increase in MyoII-GFP levels in different morphogenetic movements are different from each other. The differences in the rate changes of MyoII-GFP intensities suggest differences in the biochemical control or differences in the MyoII-associated mechanics in these movements. On one hand, different rate changes may arise from differential regulation of Rho1 activation through cell surface receptors

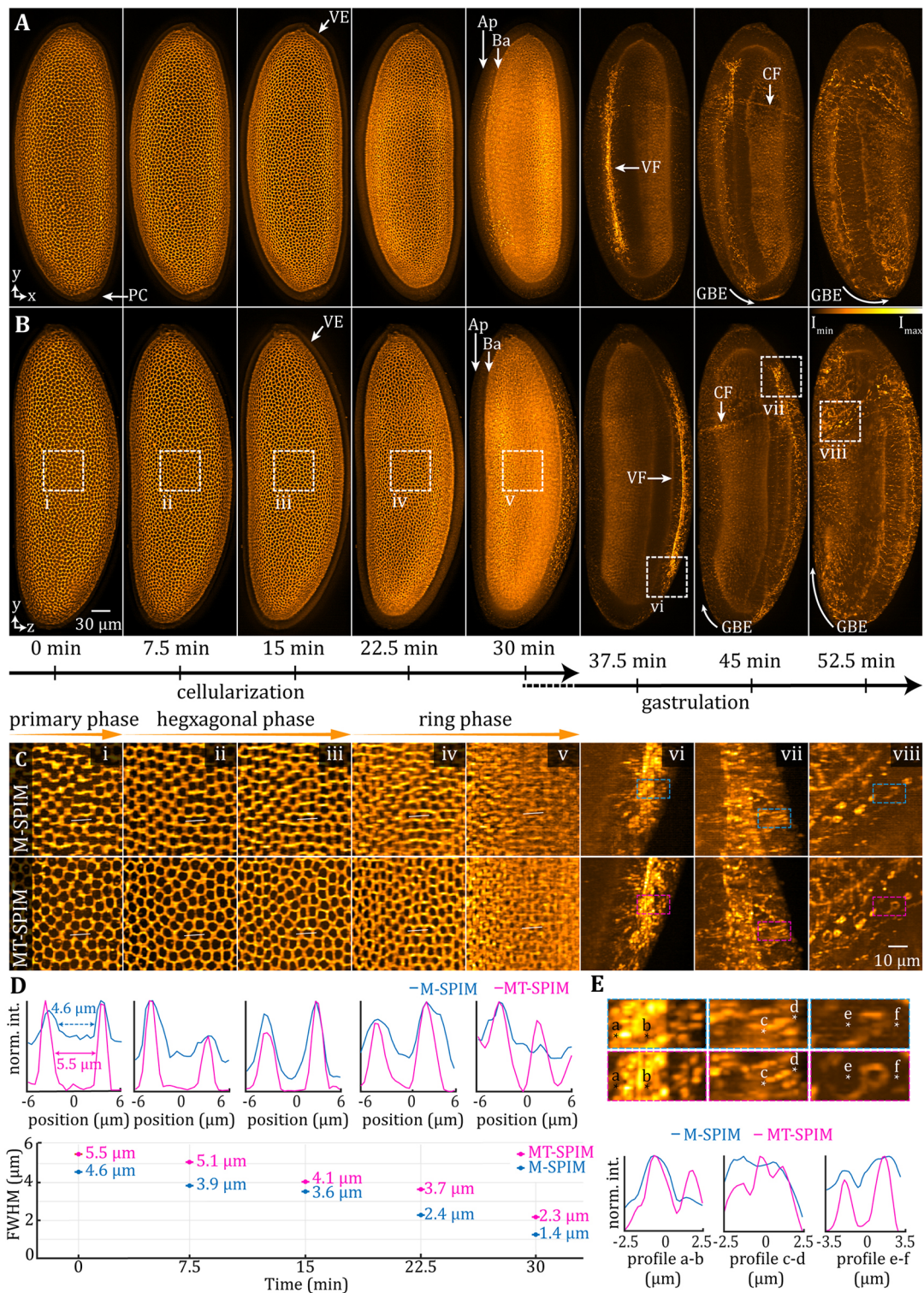


Fig. 3. Side-by-side comparison of axial resolution performance from MT-SPIM and conventional M-SPIM mode in live 3D imaging. (A) Maximum intensity projection of images (xy plane) recording MyoII-GFP during the early development of the *Drosophila* embryo in the MT-SPIM mode. A temporal series is shown (from left to right) representing embryonic stages from cellularization to the onset of the germband extension. (B) Reconstructed axial views of the images in A. The arrows highlight different regions of the embryo: PC, pole cells; VE, vitelline envelope; Ap, apical aspect of the cells; Ba, basal aspect of the cells; VF, ventral furrow formation; CF, cephalic furrow formation; GBE, germband extension. (C) Magnified regions of interests (ROIs) (i-viii) from the boxed areas in B to compare the performance of MT-SPIM and M-SPIM when reconstructing the axial resolution of the live imaging. (D) Comparison of normalized intensity profiles from the images in C. The pink and blue lines show the profile intensity of the selected line from MT-SPIM and M-SPIM (white lines in C), and the space between the two peaks shows the distance of two opposite cell contacts. The average of the measured distance indicates a larger separation (about 1 μm) between two opposite cell contacts from the MT-SPIM method compared with the M-SPIM method. (E) Enlarged views of boxed areas in Cvi-viii. Graphs show the capability of the MT-SPIM compared with conventional M-SPIM to reconstruct the nmMyoII-GFP accumulation in ventral furrow formation and contractile ring formation during cell division. Representative data from multiple independent experiments ($n=3$) are shown.

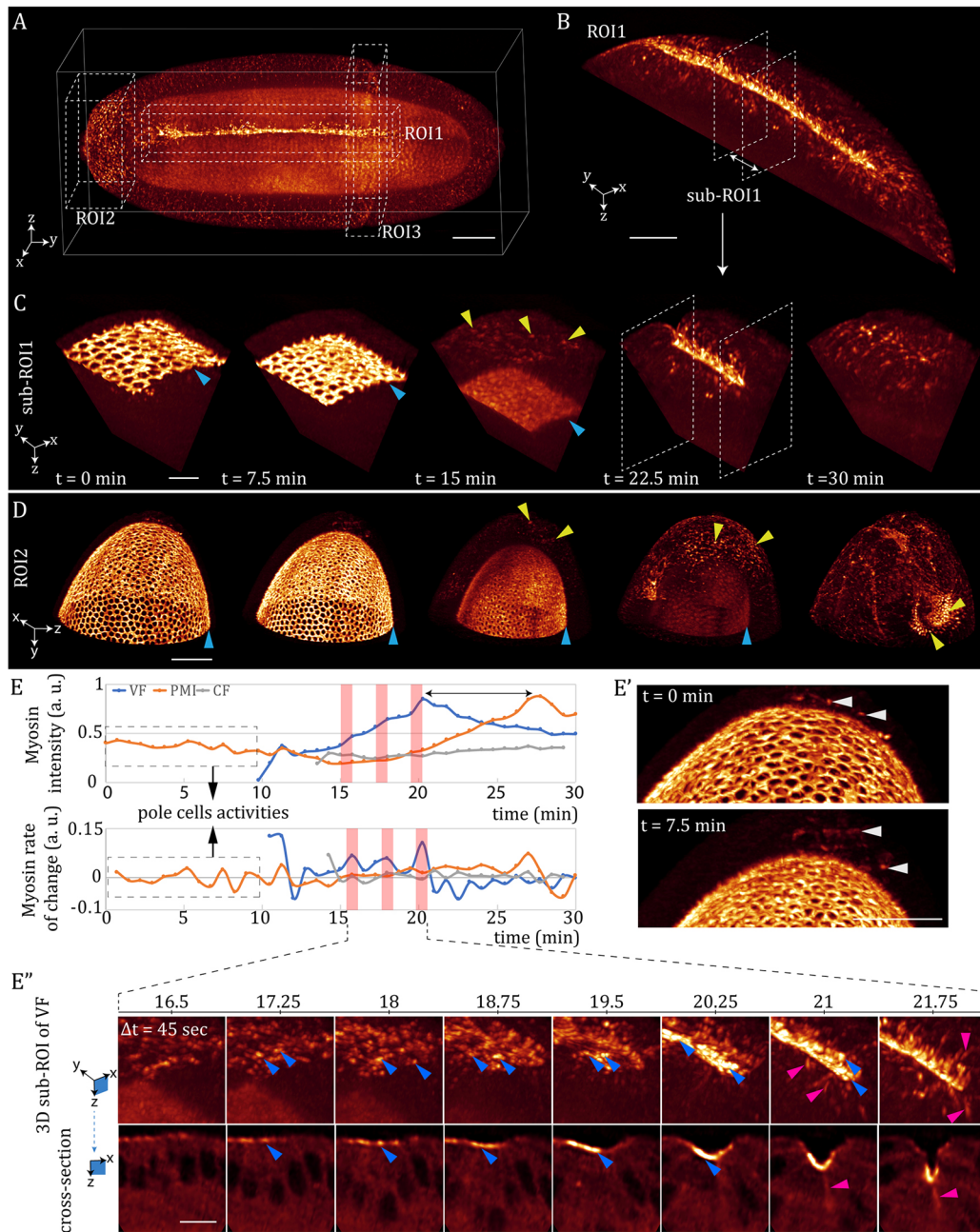


Fig. 4. The capability of the MT-SPIM for simultaneous 4D quantitative data analysis of subcellular MyoII-GFP distribution during *Drosophila* gastrulation. (A) 3D rendering of the whole *Drosophila* embryo with MyoII-GFP recorded with MT-SPIM using six tiled light sheets. Three regions of interest are selected for simultaneous investigation: ROI1, ventral furrow; ROI2, posterior midgut; ROI3, cephalic furrow. (B) MyoII dynamics on the ventral side during furrow formation visualized by a cropped 3D region of interest in A. The bright line, which is elongated from anterior to posterior, shows the MyoII-GFP accumulation from apically constricting cells in the center of the ventral furrow formation. (C) 3D region of interest from the middle part of B during embryo development. This sub-region of interest illustrates embryo development from cell formation and early gastrulation. The basal domains of the cells are indicated by the blue arrowheads, indicating the MyoII movement from apical to basal. The yellow arrowheads indicate the MyoII activity in the apical domain of the cells coinciding with end of the cell formation. (D) 3D region of interest from the posterior side of the embryo during cellularization and early gastrulation. The blue arrowheads show the basal part of the cells during cellularization; the yellow arrowheads indicate the myosin activity in the apical part of cells in the posterior. (E) The quantification of the myosin intensity in 4D for the apical side of the cells for the three regions of interests (ROI1, ROI2 and ROI3) of the embryo in A-D. The top graph shows the mean value of the MyoII-GFP fluorescence intensity at the apical domain of the cells for each ROI (the basal part is excluded); the bottom graph describes the MyoII-GFP rate of change along the time. The first 10 min of the recorded data is indicated with a dashed rectangle in the graph. This part shows that the only signal that can be extracted at this time is related to the pole cell activities in the posterior side of the embryo (see white arrows in E'). The intensity in the apical part of the ventral side is increased with a specific oscillation frequency. The pink areas in the graphs show the peaks of myosin activity during the early gastrulation, which is indicated in detail in E''. (E') Small ROI from the posterior area of the embryo. (E') Top: the 3D rendering of the myosin activities in a small part of the ventral side during the ventral furrow formation. Bottom: a cross-section image in the x-z plane taken from the center area of the images depicted in the top panels. The bright spots, which are indicated with the blue arrowheads, are the medial myosin on the apical side. The pink arrowheads also indicate some of the myosin-like cable structures necessary for apico-basal traction for ventral furrow invagination. Scale bars: 50 μ m for A,B,D,E'; 10 μ m for the C,E''. Representative data from multiple independent experiments ($n=3$) are shown.

(Kerridge et al., 2016; Manning and Rogers, 2014). On the other hand, differences in the biomechanics may be due to the distinct geometries of the position where the fluctuations occur within the embryo. In case of ventral furrow formation, it was striking that the rate changes reflect a similar timing as the reported pulsed contractions that drive this process (Martin et al., 2009). The frequencies of the rate changes were comparable with the MyoII-GFP rate changes measured by confocal microscopy. This supports the finding that the contractions are coordinated over the entire range of the ventral furrow in this phase (Martin et al., 2010).

Posterior midgut formation was reported to occur in two phases: an initial biochemical stimulation of MyoII contractions followed by a propagation wave of MyoII contractions in response to mechanical stress (Bailles et al., 2019). The whole embryo dynamic imaging revealed the bi-phasic MyoII-GFP accumulation during posterior midgut invagination and its associated subcellular MyoII-GFP structures (Fig. S7; Movie 5). In the first phase, MyoII-GFP begins to accumulate apically at cell junctions in a punctate pattern. These apical MyoII-GFP punctae aggregate to form ring-like structures (Fig. S7B; Movie 5; Chanet et al., 2017). Anterior to these

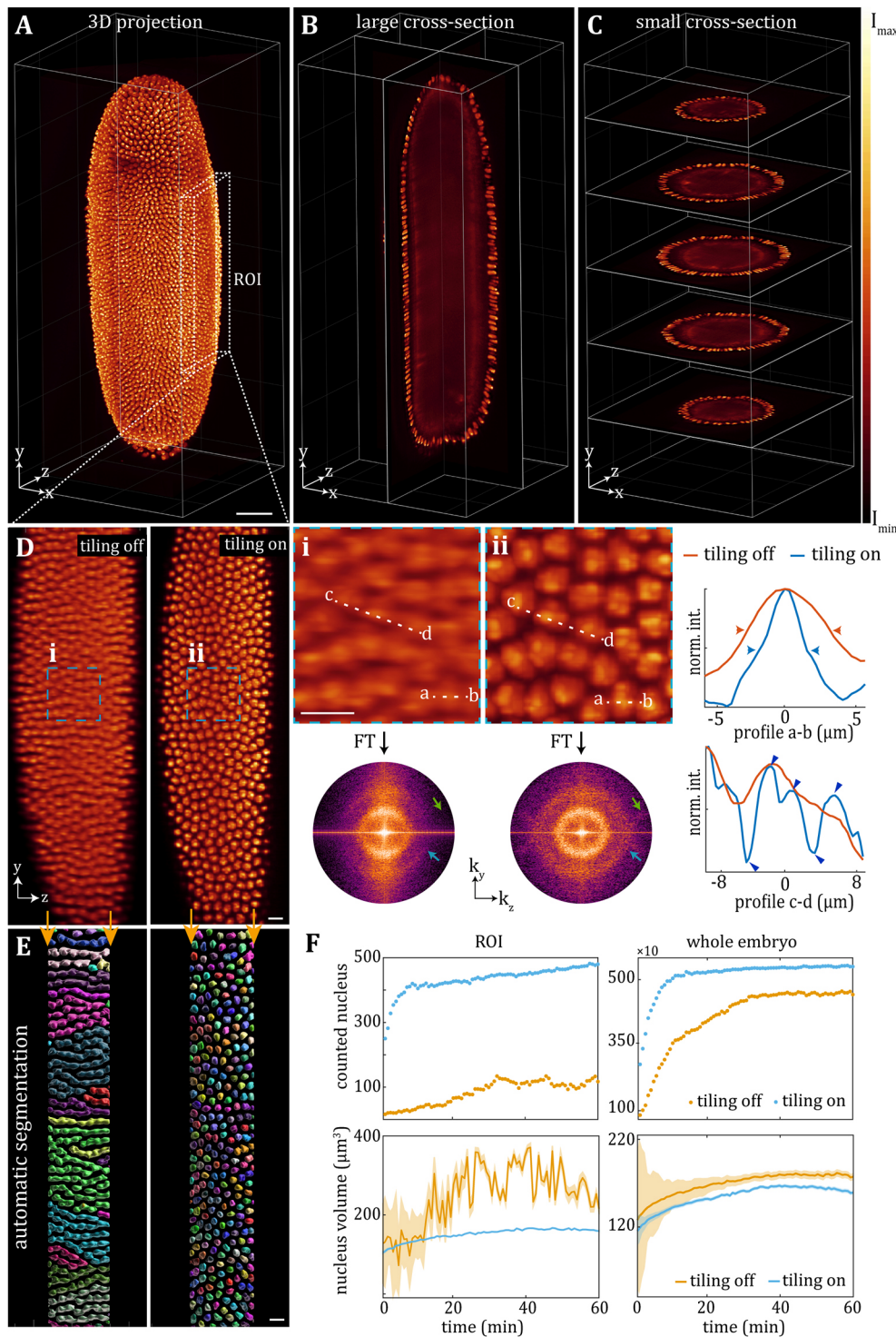


Fig. 5. The performance of the MT-SPIM in 3D imaging of the cell nucleus. (A) 3D rendering of the whole *Drosophila* embryo with His2Av-GFP. The x-y axis indicates the lateral imaging plane, and the y-z and x-z planes show the axial imaging planes. (B,C) High-quality 3D-rendered data enable us to study the different cross-sections from arbitrary views. In addition to the nuclei, His2Av-GFP can also be seen in lipid droplets beneath the cortical cytoplasm. (D) A region of interest (ROI1) from A is selected for the first step of the resolution analysis over the axial view for both Multiview imaging modes: tiling and non-tiling. (D,i,D,ii) Higher magnification of the dashed rectangular regions are provided to show the differences between the reconstructed data from both imaging modes. The intensity analysis shows that, when the tiling mode is turned on, the size of each nucleus is reconstructed 1.5 times smaller compared with the non-tiling light sheet, which demonstrates the ability of the tiling mode to distinguish the adjacent nucleus. In addition, the Fourier analysis verifies the resolution enhancement over the axial direction when the tiling mode is applied. (E) 3D-automatic segmentation of the central part of the images in D is provided to illustrate the effect of the resolution on automatic segmentation. (F) The number of the nucleus and the volume of each nucleus is also calculated based on the automatic segmentation for ROI1 and whole embryo over cellularization. Representative data from multiple independent experiments ($n=3$) are shown. Scale bars: 50 μm for A-C; 10 μm for D-E.

ring-like structures, MyoII accumulation propagates in adjacent anterior cells, which form large amorphous MyoII-GFP aggregates. Because of the complicated geometry at the poles of the embryo and the speed of this dynamic process, imaging of posterior midgut invagination by MT-SPIM provides a good example of its improved temporal-spatial resolution.

Live quantitative imaging of nuclei forming during cellularization in the *Drosophila* embryo by MT-SPIM

We next examined whether the performance of the MT-SPIM is sufficient for the imaging and segmentation of the nuclei in the entire embryo. To investigate the effect of the improved resolution on the reconstruction of the nuclei, we imaged a 2-h-old *Drosophila* embryo expressing His2Av-GFP by MT-SPIM and M-SPIM simultaneously with six tiled light sheets. His2Av-GFP is also found within more central areas of the embryo, where it is present in lipid droplets that store histones for early embryogenesis (Fig. 5B; Movie 6) (Li et al., 2012). The Multiview image fusion allows us to reconstruct the nuclei of the embryo from any arbitrary plane, such as long and small cross-sections (Fig. 5A-C; Movie 6). However, the nuclear shape and the border between them were obscured in M-SPIM data along the axial direction. In contrast to the M-SPIM, the MT-SPIM is able to resolve individual nuclei even from an axial view. Therefore, the quality of the reconstructed nuclei is completely dependent on the area selected for the analysis and, for example, the nucleus located in the axial imaging view cannot be distinguished easily as an individual nucleus using the M-SPIM method (Fig. 5D). To explore the effect of the improved resolution, the data recorded from either SPIM set-up were segmented based on the automatic thresholding algorithm. The segmentation was carried out for a region of interest (ROI) and the whole embryo over the cell formation (Fig. 5E). The results show that the two imaging modes predict different numbers of nuclei in the embryo. The number of the nuclei within the ROI is about five times higher in data based on the tiling mode compared with the conventional imaging mode. We also measured each nuclei volume for the ROI and whole embryo. The results show that the volume measurement is also dependent on the quality of the segmented nuclei. The averaged nuclei volume by the conventional light sheet was measured between $135 \pm 275 \mu\text{m}^3$ and $176 \pm 10 \mu\text{m}^3$ over cellularization, compared with the measurements based on the MT-SPIM data that were between $122 \pm 20 \mu\text{m}^3$ and $160 \pm 4 \mu\text{m}^3$. The lower standard deviation in the MT-SPIM data shows that more volume nuclei are clustered around the average size, while the M-SPIM data shows a larger error in measuring nuclei volume over cellularization, which is caused by the poor axial resolution. We conclude that the quality of the image reconstruction of M-SPIM versus MT-SPIM data can differ to an extent that may directly affect the biological interpretation.

Conclusions

MT-SPIM provides a rotation-free and compact optical setup for simultaneous subcellular and cellular imaging of a multicellular and opaque living organism. This approach supports the determination of the characteristics of a subcellular organelle inside the region of interest of the sample, as well as its dynamic changes over time in various regions of the sample. We have optimized the spatial resolution of the MT-SPIM by using a fast SLM that allows the tiling of the confined light sheet over the imaging FOV, which also enables us to achieve high-speed illumination in a near-simultaneous fashion. One benefit of the tiling approach over the conventional non-tiling mode is that the sample is protected from unwanted drift during imaging, which is required for obtaining a high-resolution image.

In addition, no time-consuming image alignment and registration is required to reconstruct the high-resolution 3D image. With the given spatial and temporal resolution, we have shown that we are able to record dynamics of proteins such as Myosin II on a subcellular scale within the whole *Drosophila* embryo without the need to rotate the sample. Additionally, we demonstrate that the MT-SPIM data can be easily coupled with automated segmentation to obtain a more accurate and complete prediction of the volume and number of nuclei in early embryos. We propose that, in the future, the MT-SPIM can be improved by combining this technique with adaptive optics (Royer et al., 2016) and smart microscopy (He and Huysken, 2020) to achieve a further increased image resolution in order to achieve novel insight into the dynamic control of cell and tissue interactions.

MATERIALS AND METHODS

Multiview tiling-SPIM microscope configuration

In the proposed Multiview tiling-SPIM, a diode laser with 488 nm wavelength operates as an illumination source to excite the GFP-based sample (Fig. S8). A ~ 1 mm output diameter of a laser beam is insufficient to interact with a spatial light modulator (SLM) (SXGA-3DM-DEV Microdisplay device, Forth dimension displays) with a diameter of ~ 12 mm. As a result, the laser beam is expanded to a diameter of 12 mm using a two-lens telescope configuration (L1, focal length (f)=25 mm; L2, f =300 mm) to cover the entire region of the SLM for efficient beam shaping. The reflected light from the SLM is then passed through a lens (L3: f =100 mm), resulting in a Fraunhofer diffraction pattern in its Fourier plane. The unwanted diffraction components caused by the inherent pixelated SLM structure are filtered by a pinhole. Following the pinhole, the filtered light is collected by another lens (L4: f =75 mm) to create a conjugation of the pattern projected by the SLM. The light then hits a series of optical components, including a Z-Galvo mirror, two lenses, a Y-Galvo mirror and a Fourier transforming lens. The Z-Galvo mirror (GVS412/M, Thorlabs) is used to reposition the illumination light through the sample for volume imaging, which is conjugated to the Y-Galvo mirror (GVS412/M, Thorlabs) by the lens pair to create the light sheet. The primary light sheet is detectable in the focal length of the Fourier transforming lens (L6: f =75 mm) positioned in front of the Y-Galvo mirror. The primary light sheet is divided by a knife edge mirror (MRAK25-G01, Thorlabs) to direct the light sheet into the right and left illumination arms in order to achieve two side illumination. The shaped primary light sheet is then collected by a lens (L7, f =150 mm) and an objective lens (N10xW-PF, 0.3 NA, 3.5 mm WD, Nikon) assembly, which guides the light sheet to the chamber to excite a particular layer of the sample. The emitted light is then collected from two directions at the same time by two objective lenses (20xW, Water, 0.5 NA, UMPLFLN, Olympus). A quick piezo positioner is used to align the imaging objective lenses with the position of the light sheet (P-625.1CD, PI derived by E-709.CHG). The collected light is then imaged on a single sCMOS camera (Orca-flash 4.0 V2, Hamamatsu) with a knife edge mirror and a combination of two tube lenses (U-TLU-1-2, f =200 mm Olympus).

Multi-tiled light sheet based on SLM

To enable the SLM to be used for tiling, it is encoded with several patterns that allow the focal point of the light sheet to be shifted along the direction of the beam propagation. The SLM operates on the basis of a digital pattern referred to as a hologram, which is usually synthesized digitally. Specifically designed for tiling, a digital hologram is a pattern that behaves as a lens. The ability to encrypt a lens into a programmable SLM is appealing as the focal length of the lens can be varied at the frame rate of the SLM, allowing access to a rapidly tunable lens. To implement this method and create the tiling light sheet, we used the SSPIM toolbox to create digital holograms based on virtual lenses (Aakhte et al., 2018).

Microscope control and operating system

In order to perform high-speed imaging, the Multiview tiling-SPIM is controlled by a fast programmable gate array (FPGA) (PCIe-7851 Multifunction Reconfigurable I/O Device, National instrument) (Figs S9 and S10). The microscope is controlled with a home-built graphical user

interface (GUI) based on LabView 64-bit which is running on a high-speed computer with 128 GB random-access memory (RAM), 18 central processing units (CPU) (3 GHz) and a 8 TB solid states drive (SSD, 4x Samsung 860 EVO MZ-76E2T0B) for operating system and data storage.

Data analysis and visualization

The image post-processing and visualization of the recorded data are carried out in four steps. In the first step, the effective field of view of each tiled light sheet is cropped for each time point using a scripted macro in the Fiji environment (Schindelin et al., 2012). For example, for six-tile light-sheet imaging, the cropping should be repeated six times (Fig. S3). In the second step, the cropped volume images are aligned and stitched together with the BigStitcher plug-in (Hörl et al., 2019) in Fiji. Then, in order to gain the resolution, the fused data are deconvolved with the Lucy-Richardson method using a GPU-based plug-in that is called CLIJ (Haase et al., 2020). The final data visualization and segmentation is carried out with Fiji and Imaris 9.5 together.

Drosophila culture and sample preparation

Drosophila melanogaster stocks were raised on cornmeal-based media following standard procedures. Embryos were collected on yeasted apple juice plates between 2 and 3 h after egg-laying. The embryos were dechorionated with 50% commercial bleach for around 2 min followed by careful rinsing in tap water. Several embryos were selected and submersed into 1.5% low melting agarose in phosphate-buffered saline (PBS) and rapidly transferred into a glass capillary with an inner diameter of 800 µm. The capillary was mounted to a holder and inserted into the imaging chamber. The temperature during imaging was 22°C. All embryos shown in this work were further cultured after imaging and hatched to first instar larvae. The following stocks were obtained from the Bloomington *Drosophila* Stock Center: y^1 , w^{1118} , cv^1 , sqh^{AX3} ; $P\{w[+mC]=sqh-GFP.RLC\}2His2Av-EGFP.C\}2/Sm6a$ and $w[*]$; $P\{w[+mC]=His2Av-EGFP.C\}2/SM6a$. The *His2Av-EGFP* marker was introduced into a *klar¹* mutant background, which reduced diffraction of the illumination beam. The *klarsicht¹* (*klar¹*) mutation was used to reduce light diffraction during imaging of living embryos. Because of their high diffractive index and light-scattering properties, lipid droplets reduce the excitation and the emission of fluorescence in the sample. *klar¹* affects microtubule-dependent transport of lipid droplets by blocking their outward movement late in cellularization; as a result, the majority of lipid droplets is trapped in the central yolk (Welte et al., 1998). This severe reduction of lipid droplet numbers in the newly formed cells of the cellular blastoderm improves fluorescent imaging. Females homozygous for the loss-of-function allele *klar¹* are viable and fertile, and, except for the lipid droplet clouding defect, no other developmental defects have been reported in embryos obtained from *klar¹* homozygotes (Welte et al., 1998). The *ru¹*, *klar¹* stock was a gift from M. Welte (University of Rochester, NY, USA).

Acknowledgements

We thank Ehsan Ahadi Akhlaghi, Jens Januschke, Peter Lehmann and Michael Welte for discussions throughout the work, for critically reading the manuscript and for their insightful comments. We thank CINSaT (Centre of Interdisciplinary Nanostructure Science and Technology, University of Kassel) for support and discussion, and also Cristian Sarpe's support with electronic and optical measurement equipment. We thank the *Drosophila* Stock Center (Bloomington, IN, USA) for *Drosophila* stocks. We thank Birgitt Simon and Monika Winnekecht for preparing fly food, and the workshop of the Natural Science Department of the University Kassel for constructing customized devices and tools.

Competing interests

The authors declare that they have no competing interests. The University of Kassel (employer) has filed a patent application to the German Patent and Trade Mark office under file DE 10 2021 107 821.0 for the invention of the MT-SPIM microscope design and setup.

Author contributions

Conceptualization: M.A., H.-A.J.M.; Methodology: M.A.; Software: M.A.; Validation: M.A., H.-A.J.M.; Formal analysis: M.A.; Investigation: M.A., H.-A.J.M.; Resources: M.A., H.-A.J.M.; Data curation: M.A., H.-A.J.M.; Writing - original draft: M.A., H.-A.J.M.;

Writing - review & editing: M.A., H.-A.J.M.; Visualization: M.A.; Supervision: H.-A.J.M.; Project administration: H.-A.J.M.; Funding acquisition: H.-A.J.M.

Funding

This research was funded by startup funding from the Universität Kassel to H.-A.J.M.

Peer review history

The peer review history is available online at <https://journals.biologists.com/dev/article-lookup/doi/10.1242/dev.199725>

References

- Aakhte, M., Akhlaghi, E. A. and Müller, H.-A. J. (2018). SSPIM: a beam shaping toolbox for structured selective plane illumination microscopy. *Sci. Rep.* **8**, 10067. doi:10.1038/s41598-018-28389-8
- Bailles, A., Collinet, C., Philippe, J.-M., Lenne, P.-F., Munro, E. and Lecuit, T. (2019). Genetic induction and mechanochemical propagation of a morphogenetic wave. *Nature* **572**, 467-473. doi:10.1038/s41586-019-1492-9
- Chakraborty, T., Driscoll, M. K., Jeffery, E., Murphy, M. M., Roudot, P., Chang, B.-J., Vora, S., Wong, W. M., Nielson, C. D., Zhang, H. et al. (2019). Light-sheet microscopy of cleared tissues with isotropic, subcellular resolution. *Nat. Methods* **16**, 1109-1113. doi:10.1038/s41592-019-0615-4
- Chanet, S., Miller, C. J., Vaishnav, E. D., Ermentrout, B., Davidson, L. A. and Martin, A. C. (2017). Actomyosin meshwork mechanosensing enables tissue shape to orient cell force. *Nat. Commun.* **8**, 15014. doi:10.1038/ncomms15014
- Chen, B.-C., Legant, W. R., Wang, K., Shao, L., Milkie, D. E., Davidson, M. W., Janetopoulos, C., Wu, X. S., Hammer, J. A., III, Liu, Z. et al. (2014). Lattice light-sheet microscopy: imaging molecules to embryos at high spatiotemporal resolution. *Science* **346**, 1257998. doi:10.1126/science.1257998
- Chen, Y., Li, X., Zhang, D., Wang, C., Feng, R., Li, X., Wen, Y., Xu, H., Zhang, X. S., Yang, X. et al. (2020). A versatile tiling light sheet microscope for imaging of cleared tissues. *Cell Rep.* **33**, 108349. doi:10.1016/j.celrep.2020.108349
- Chhetri, R. K., Amat, F., Wan, Y., Höckendorf, B., Lemon, W. C. and Keller, P. J. (2015). Whole-animal functional and developmental imaging with isotropic spatial resolution. *Nat. Methods* **12**, 1171-1178. doi:10.1038/nmeth.3632
- Chmielewski, A. K., Kyrsting, A., Mahou, P., Wayland, M. T., Muresan, L., Evers, J. F. and Kaminski, C. F. (2015). Fast imaging of live organisms with sculpted light sheets. *Sci. Rep.* **5**, 9385. doi:10.1038/srep09385
- Dean, K. M. and Fiolka, R. (2014). Uniform and scalable light-sheets generated by extended focusing. *Opt. Express* **22**, 26141-26152. doi:10.1364/OE.22.026141
- Dean, K. M., Roudot, P., Welf, E. S., Danuser, G. and Fiolka, R. (2015). Deconvolution-free subcellular imaging with axially swept light sheet microscopy. *Biophys. J.* **108**, 2807-2815. doi:10.1016/j.bpj.2015.05.013
- Engelbrecht, C. J. and Stelzer, E. H. (2006). Resolution enhancement in a light-sheet-based microscope (SPIM). *Opt. Lett.* **31**, 1477-1479. doi:10.1364/OL.31.001477
- Fahrbach, F. O., Simon, P. and Rohrbach, A. (2010). Microscopy with self-reconstructing beams. *Nat. Photonics* **4**, 780-785. doi:10.1038/nphoton.2010.204
- Fu, Q., Martin, B. L., Matus, D. Q. and Gao, L. (2016). Imaging multicellular specimens with real-time optimized tiling light-sheet selective plane illumination microscopy. *Nat. Commun.* **7**, 11088. doi:10.1038/ncomms11088
- Gao, L. (2015). Extend the field of view of selective plane illumination microscopy by tiling the excitation light sheet. *Opt. Express* **23**, 6102-6111. doi:10.1364/OE.23.006102
- Gao, L., Shao, L., Chen, B.-C. and Betzig, E. (2014). 3D live fluorescence imaging of cellular dynamics using Bessel beam plane illumination microscopy. *Nat. Protoc.* **9**, 1083-1101. doi:10.1038/nprot.2014.087
- Gheisari, E., Aakhte, M. and Müller, H.-A. J. (2020). Gastrulation in *Drosophila melanogaster*: genetic control, cellular basis and biomechanics. *Mech. Dev.* **163**, 103629. doi:10.1016/j.mod.2020.103629
- Haase, R., Royer, L. A., Steinbach, P., Schmidt, D., Dibrov, A., Schmidt, U., Weigert, M., Maghelli, N., Tomancak, P., Jug, F. et al. (2020). CLIJ: GPU-accelerated image processing for everyone. *Nat. Methods* **17**, 5-6. doi:10.1038/s41592-019-0650-1
- He, J. and Huysken, J. (2020). Image quality guided smart rotation improves coverage in microscopy. *Nat. Commun.* **11**, 150. doi:10.1038/s41467-019-13821-y
- He, B., Martin, A. and Wieschaus, E. (2016). Flow-dependent myosin recruitment during *Drosophila* cellularization requires zygotic *dunk* activity. *Development* **143**, 2417-2430. doi:10.1242/dev.131334
- Hörl, D., Rojas Rusak, F., Preusser, F., Tillberg, P., Randel, N., Chhetri, R. K., Cardona, A., Keller, P. J., Harz, H., Leonhardt, H. et al. (2019). BigStitcher: reconstructing high-resolution image datasets of cleared and expanded samples. *Nat. Methods* **16**, 870-874. doi:10.1038/s41592-019-0501-0
- Huysken, J., Swoger, J., Del Bene, F., Wittbrodt, J. and Stelzer, E. H. K. (2004). Optical sectioning deep inside live embryos by selective plane illumination microscopy. *Science* **305**, 1007-1009. doi:10.1126/science.1100035
- Keller, P. J., Schmidt, A. D., Wittbrodt, J. and Stelzer, E. H. K. (2008). Reconstruction of zebrafish early embryonic development by scanned light sheet microscopy. *Science* **322**, 1065-1069. doi:10.1126/science.1162493

- Kerridge, S., Munjal, A., Philippe, J.-M., Jha, A., de las Bayonas, A. G., Saurin, A. J. and Lecuit, T. (2016). Modular activation of Rho1 by GPCR signalling imparts polarized myosin II activation during morphogenesis. *Nat. Cell Biol.* **18**, 261-270. doi:10.1038/ncb3302
- Krueger, D., Quinkler, T., Mortensen, S. A., Sachse, C. and De Renzis, S. (2019). Cross-linker-mediated regulation of actin network organization controls tissue morphogenesis. *J. Cell Biol.* **218**, 2743-2761. doi:10.1083/jcb.201811127
- Krzic, U., Gunther, S., Saunders, T. E., Streichan, S. J. and Hufnagel, L. (2012). Multiview light-sheet microscope for rapid *in toto* imaging. *Nat. Methods* **9**, 730-733. doi:10.1038/nmeth.2064
- Ladoux, B. and Mège, R.-M. (2017). Mechanobiology of collective cell behaviours. *Nat. Rev. Mol. Cell Biol.* **18**, 743-757. doi:10.1038/nrm.2017.98
- Li, Z., Thiel, K., Thul, P. J., Beller, M., Kühnlein, R. P. and Welte, M. A. (2012). Lipid droplets control the maternal histone supply of *Drosophila* embryos. *Curr. Biol.* **22**, 2104-2113. doi:10.1016/j.cub.2012.09.018
- Manning, A. J. and Rogers, S. L. (2014). The Fog signaling pathway: insights into signaling in morphogenesis. *Dev. Biol.* **394**, 6-14. doi:10.1016/j.ydbio.2014.08.003
- Martin, A. C., Kaschube, M. and Wieschaus, E. F. (2009). Pulsed contractions of an actin-myosin network drive apical constriction. *Nature* **457**, 495-499. doi:10.1038/nature07522
- Martin, A. C., Gelbart, M., Fernandez-Gonzalez, R., Kaschube, M. and Wieschaus, E. F. (2010). Integration of contractile forces during tissue invagination. *J. Cell Biol.* **188**, 735-749. doi:10.1083/jcb.200910099
- Miao, H. and Blankenship, J. T. (2020). The pulse of morphogenesis: actomyosin dynamics and regulation in epithelia. *Development* **147**, dev186502. doi:10.1242/dev.186502
- Nyilk, J., McCluskey, K., Aggarwal, S., Tello, J. A. and Dholakia, K. (2016). Enhancement of image quality and imaging depth with Airy light-sheet microscopy in cleared and non-cleared neural tissue. *Biomed. Opt. Express* **7**, 4021-4033. doi:10.1364/BOE.7.004021
- Pitrone, P. G., Schindelin, J., Stuyvenberg, L., Preibisch, S., Weber, M., Eliceiri, K. W., Huisken, J. and Tomancak, P. (2013). OpenSPIM: an open-access light-sheet microscopy platform. *Nat. Methods* **10**, 598-599. doi:10.1038/nmeth.2507
- Planchon, T. A., Gao, L., Milkie, D. E., Davidson, M. W., Galbraith, J. A., Galbraith, C. G. and Betzig, E. (2011). Rapid three-dimensional isotropic imaging of living cells using Bessel beam plane illumination. *Nat. Methods* **8**, 417-423. doi:10.1038/nmeth.1586
- Remacha, E., Friedrich, L., Vermot, J. and Fahrbach, F. O. (2020). How to define and optimize axial resolution in light-sheet microscopy: a simulation-based approach. *Biomed. Opt. Express* **11**, 8-26. doi:10.1364/BOE.11.000008
- Royer, L. A., Lemon, W. C., Chhetri, R. K., Wan, Y., Coleman, M., Myers, E. W. and Keller, P. J. (2016). Adaptive light-sheet microscopy for long-term, high-resolution imaging in living organisms. *Nat. Biotechnol.* **34**, 1267-1278. doi:10.1038/nbt.3708
- Schejter, E. D. and Wieschaus, E. (1993). Functional elements of the cytoskeleton in the early *Drosophila* embryo. *Annu. Rev. Cell Biol.* **9**, 67-99. doi:10.1146/annurev.cb.09.110193.000435
- Schindelin, J., Arganda-Carreras, I., Frise, E., Kaynig, V., Longair, M., Pietzsch, T., Preibisch, S., Rueden, C., Saalfeld, S., Schmid, B. et al. (2012). Fiji: an open-source platform for biological-image analysis. *Nat. Methods* **9**, 676-682. doi:10.1038/nmeth.2019
- Streichan, S. J., Lefebvre, M. F., Noll, N., Wieschaus, E. F. and Shraiman, B. I. (2018). Global morphogenetic flow is accurately predicted by the spatial distribution of myosin motors. *eLife* **7**, e27454. doi:10.7554/eLife.27454
- Tomer, R., Khairy, K., Amat, F. and Keller, P. J. (2012). Quantitative high-speed imaging of entire developing embryos with simultaneous multiview light-sheet microscopy. *Nat. Methods* **9**, 755-763. doi:10.1038/nmeth.2062
- Truong, T. V., Supatto, W., Koos, D. S., Choi, J. M. and Fraser, S. E. (2011). Deep and fast live imaging with two-photon scanned light-sheet microscopy. *Nat. Methods* **8**, 757-760. doi:10.1038/nmeth.1652
- Tsai, Y.-C., Tang, W.-C., Low, C. S. L., Liu, Y.-T., Wu, J.-S., Lee, P.-Y., Chen, L. Q., Lin, Y.-L., Kanchanawong, P., Gao, L. et al. (2020). Rapid high resolution 3D imaging of expanded biological specimens with lattice light sheet microscopy. *Methods* **174**, 11-19. doi:10.1016/j.ymeth.2019.04.006
- Vettenburg, T., Dalgarno, H. I. C., Nyilk, J., Coll-Lladó, C., Ferrier, D. E. K., Čížmár, T., Gunn-Moore, F. J. and Dholakia, K. (2014). Light-sheet microscopy using an Airy beam. *Nat. Methods* **11**, 541-544. doi:10.1038/nmeth.2922
- Voigt, F. F., Kirschenbaum, D., Platonova, E., Pagès, S., Campbell, R. A. A., Kastli, R., Schaettin, M., Egolf, L., van der Bourg, A., Bethge, P. et al. (2019). The mesoSPIM initiative: open-source light-sheet microscopes for imaging cleared tissue. *Nat. Methods* **16**, 1105-1108. doi:10.1038/s41592-019-0554-0
- Wang, D., Jin, Y., Feng, R., Chen, Y. and Gao, L. (2019). Tiling light sheet selective plane illumination microscopy using discontinuous light sheets. *Opt. Express* **27**, 34472-34483. doi:10.1364/OE.27.034472
- Welte, M. A., Gross, S. P., Postner, M., Block, S. M. and Wieschaus, E. F. (1998). Developmental regulation of vesicle transport in *Drosophila* embryos: forces and kinetics. *Cell* **92**, 547-557. doi:10.1016/S0092-8674(00)80947-2
- Yang, Z., Prokopas, M., Nyilk, J., Coll-Lladó, C., Gunn-Moore, F. J., Ferrier, D. E. K., Vettenburg, T. and Dholakia, K. (2014). A compact Airy beam light sheet microscope with a tilted cylindrical lens. *Biomed. Opt. Express* **5**, 3434-3442. doi:10.1364/BOE.5.003434

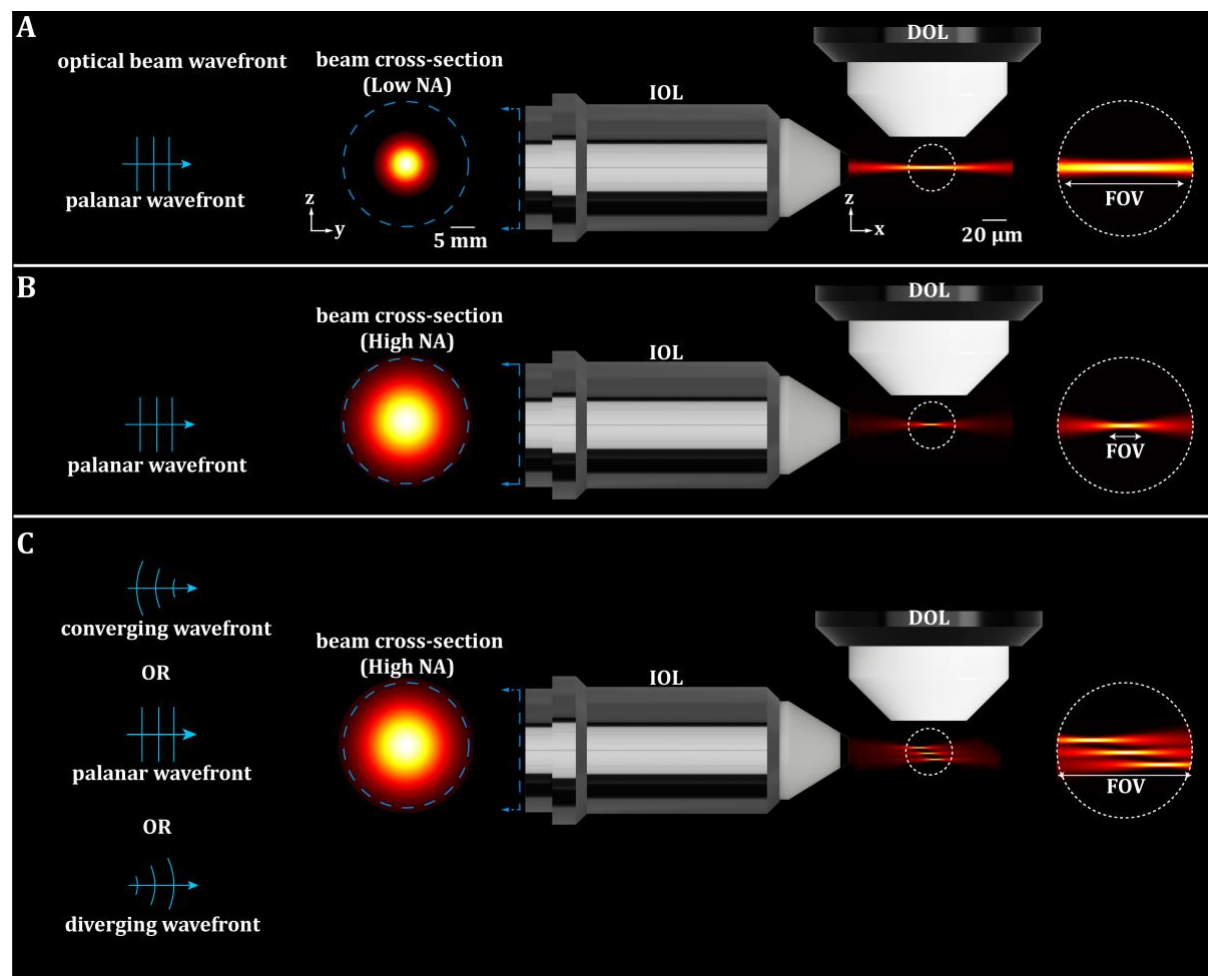


Fig. S1. Light sheet thickness and its effective field of view. The size of the light sheet at the sample plane is proportional to the diameter of the illumination beam at the rear pupil of the illumination objective lens (IOL). (A) A narrower diameter illumination beam at the IOL's rear pupil produces a thick centered beam with a wide field of view (FOV). (B) A greater diameter light beam at the IOL's rear pupil results in a thinner and smaller FOV at the sample plane. (C) By slightly changing the wavefront of the illumination beam in the IOL's rear pupil, the thin light sheet can be tiled over the broad FOV.

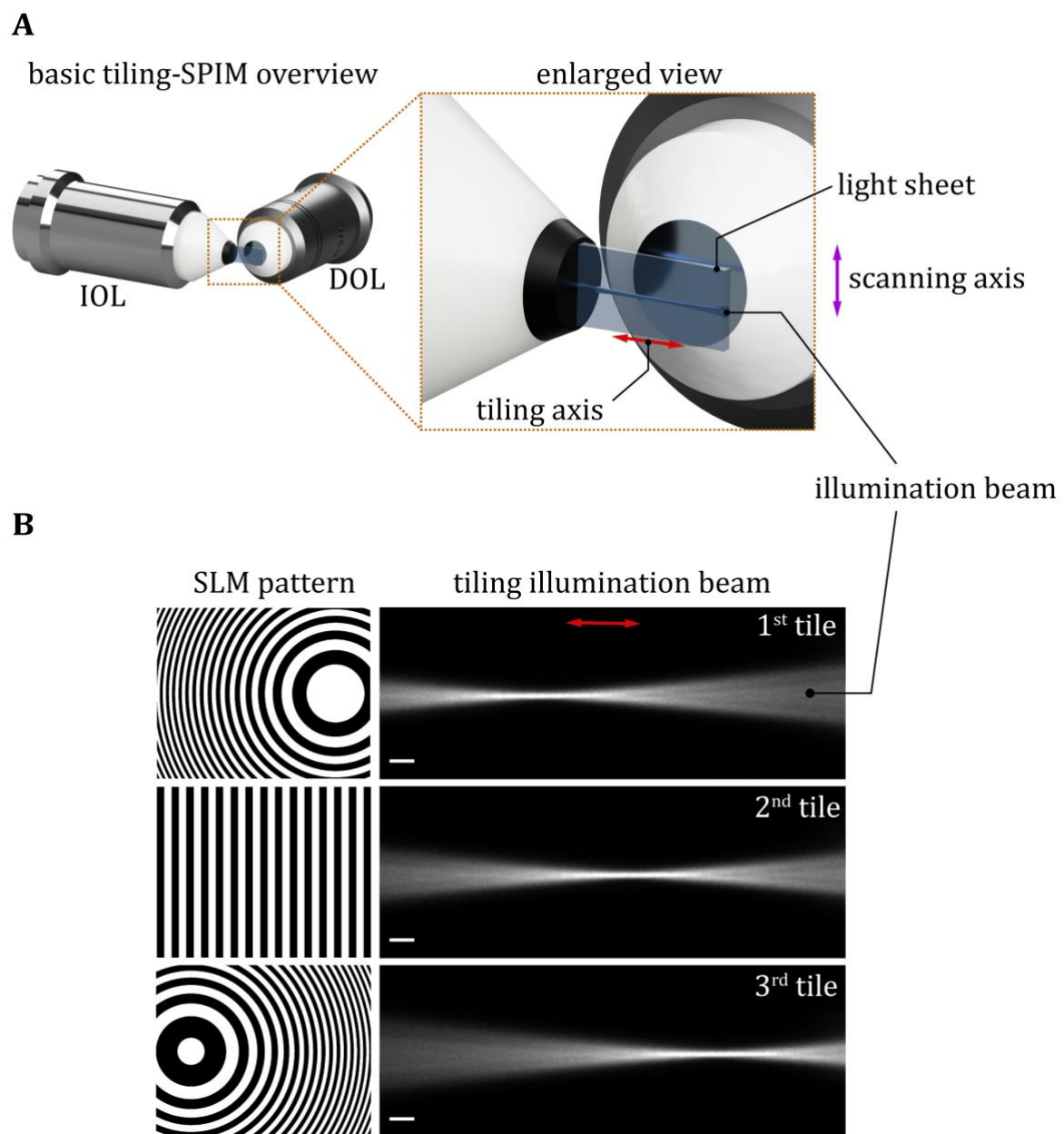


Fig. S2. The tiling technique is depicted in the SPIM simple setup. (A) The basic SPIM configuration with two objective lenses. (B) The left column depicts three distinct SLM patterns based on virtual lenses with various focal lengths, and the right column depicts the recorded the tiled illumination beams through the dye solution. Scale bars, 10 μm .

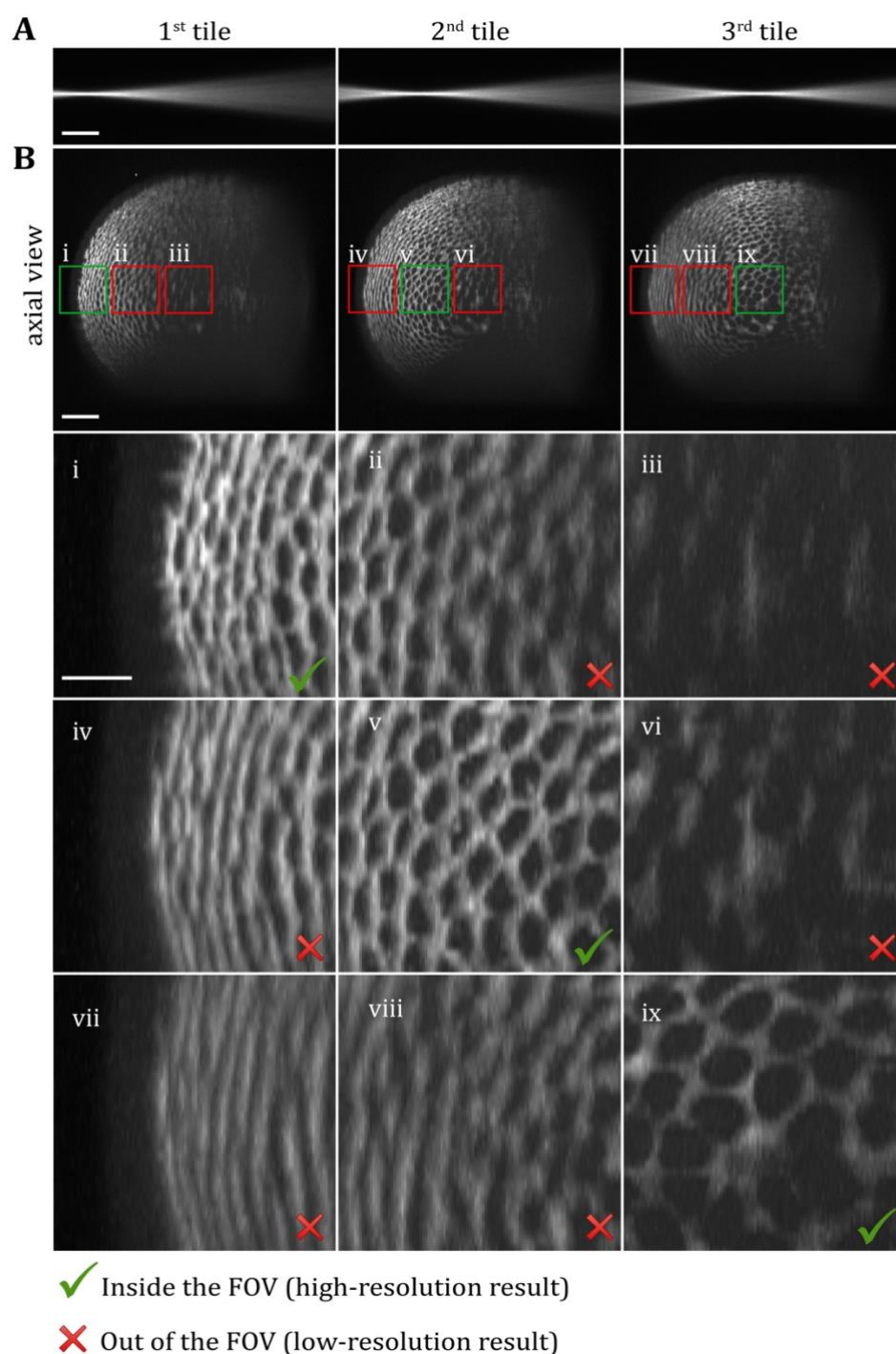


Fig. S3. The performance of the Basic tiling-SPIM with two objective lenses for imaging an opaque sample. (A) Tiled illumination beam through dye solution. (B) A reconstructed axial view of a recorded *Drosophila* embryo for each tiled light sheet is shown (A). The green marked area represented the maximum axial resolution on each tiled light sheet, which should be considered for the final image reconstruction. The scale bars for A and B are 30 μ m and 10 μ m for the subset images (i-ix).

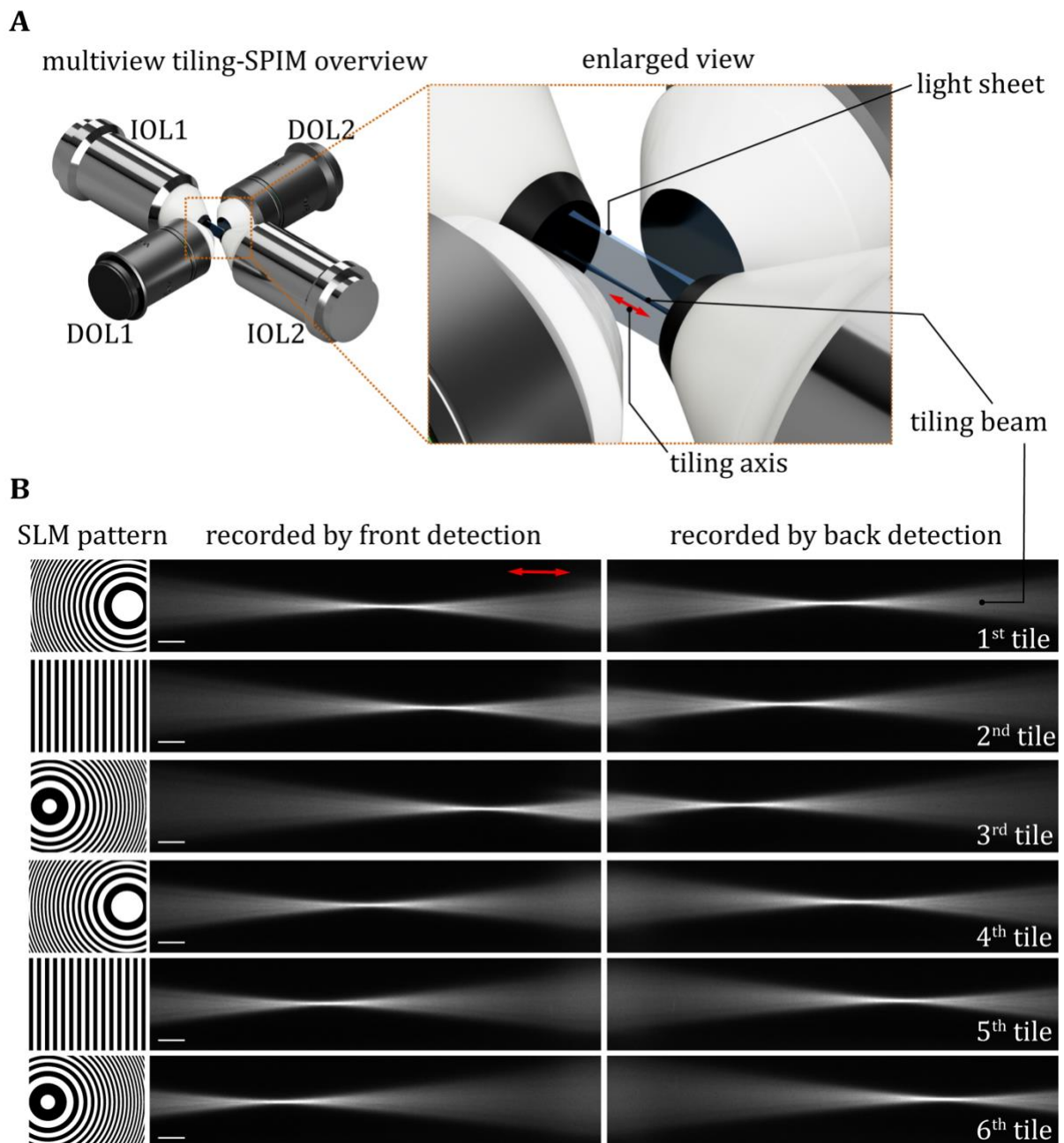


Fig. S4. The tiling technique is depicted based on the Multiview-SPIM setup. (A) The Multiview-SPIM configuration with four objective lenses; two illumination objective lenses (IOL) and two detection objective lenses (DOL). (B) The left column depicts six distinct SLM patterns based on virtual lenses with various focal lengths, and the two right columns depict the recorded tiled illumination beams via two detection arms simultaneously. Scale bars, 20 μm.

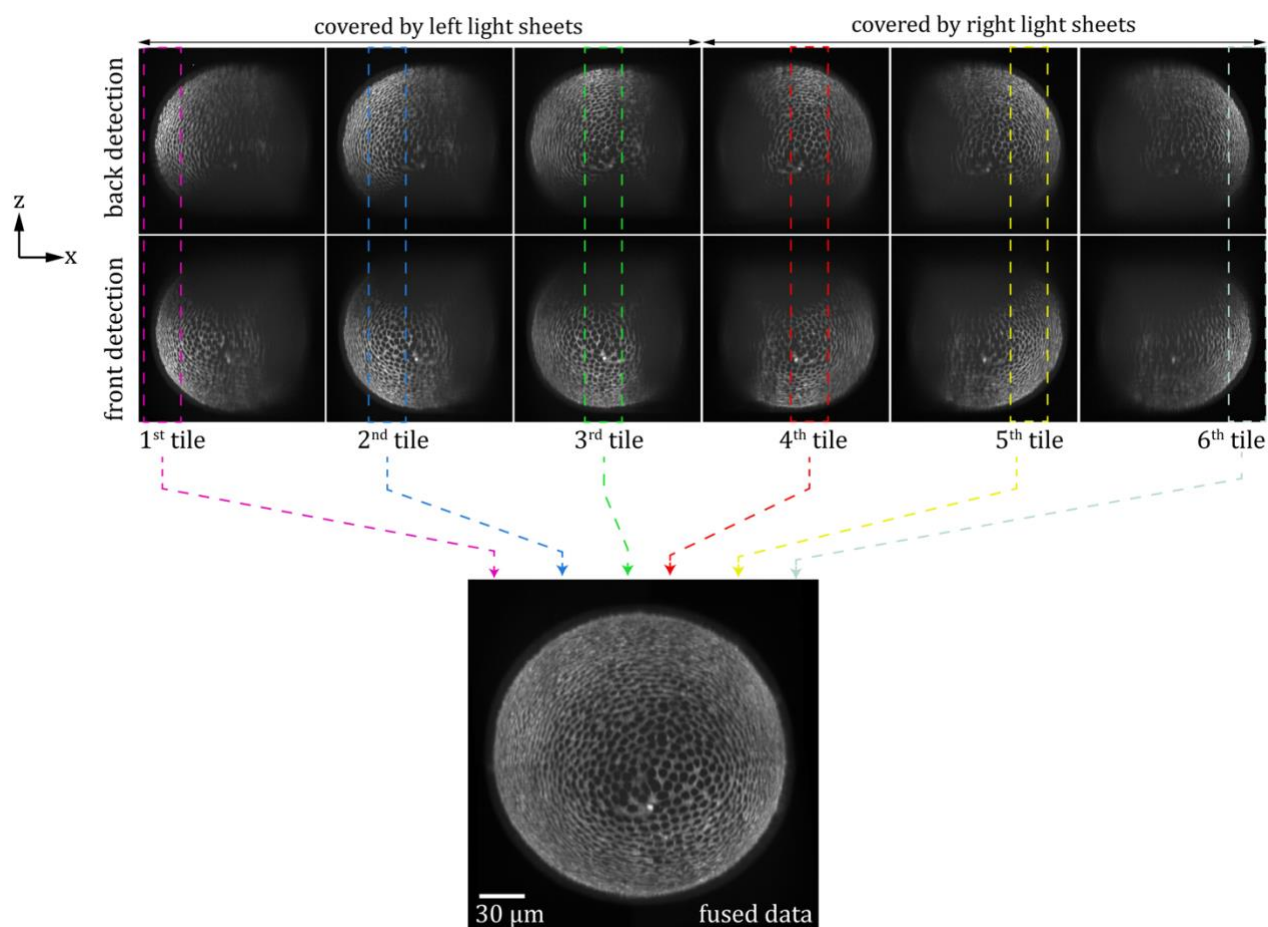


Fig. S5. The performance of the MT-SPIM for imaging an opaque sample (A) The recorded data with MT-SPIM by six tiles is composed of 12 volume images per single time point which are illuminated with multi-tiled light sheets and recorded from multi views. All views show axial views of the raw imaged based on maximum intensity projection (MIP) and each part of the sample that is illuminated with the particular tiled light sheet is indicated with color-coded dashed boxes. (B) The MIP of the reconstructed axial view.

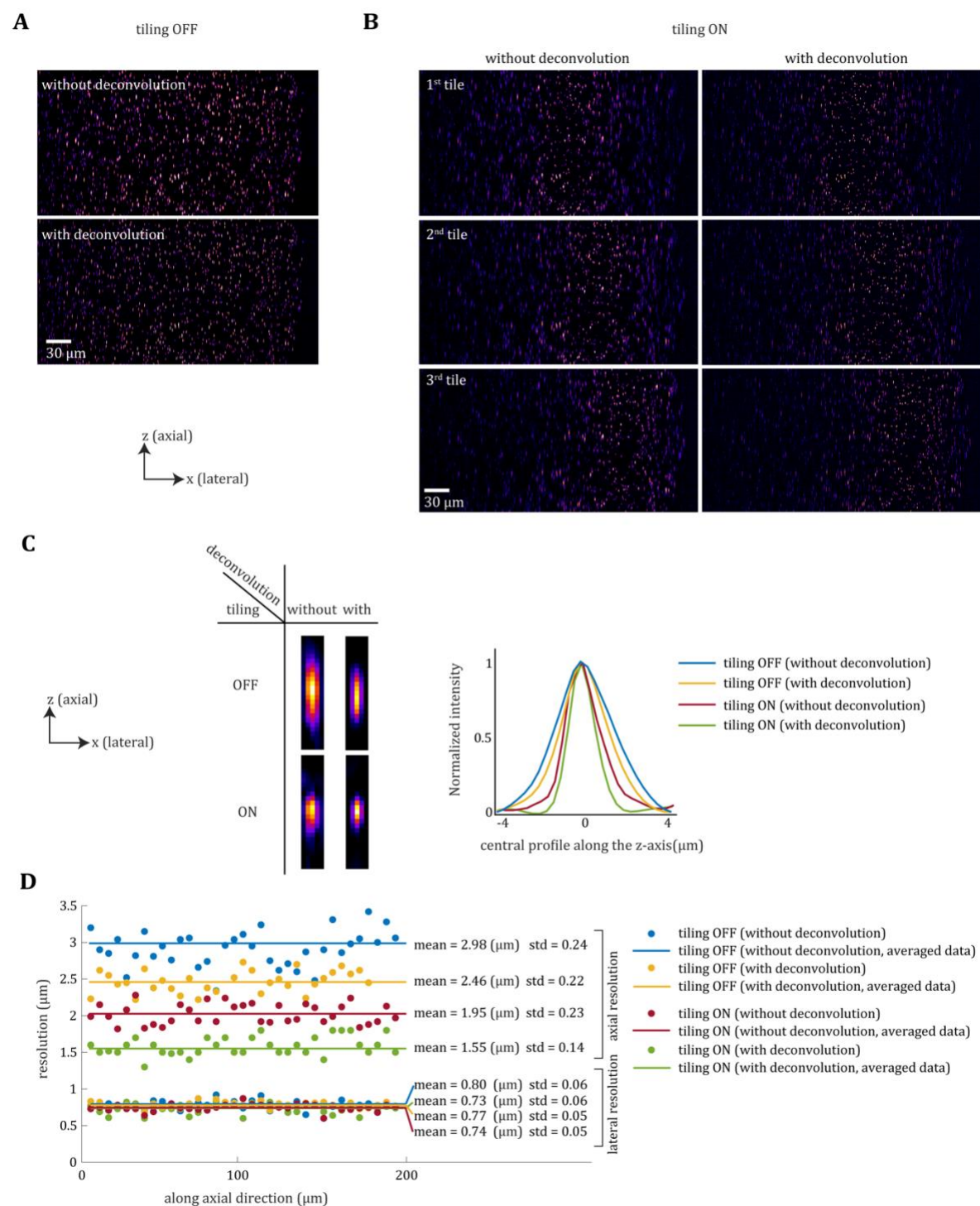


Fig. S6. SPIM experimental point spread function measurement comparing non-tiling SPIM vs tiling SPIM. The axial resolution of the microscope was determined by imaging 400 nm diameter fluorescent microspheres. **(A)** The axial view of microspheres imaged in the non-tiling SPIM mode. **(B)** The axial view of the microspheres imaged by the tiling SPIM mode. **(C)** An enlarged image of one of the imaged microspheres in two modes, as well as with and without deconvolution. The right plot depicts the center axial intensity distribution of the left images. **(D)** This graph summarizes the full width at half maxima of the microspheres ($n=30$) across 200 μm along the axial and lateral axes.

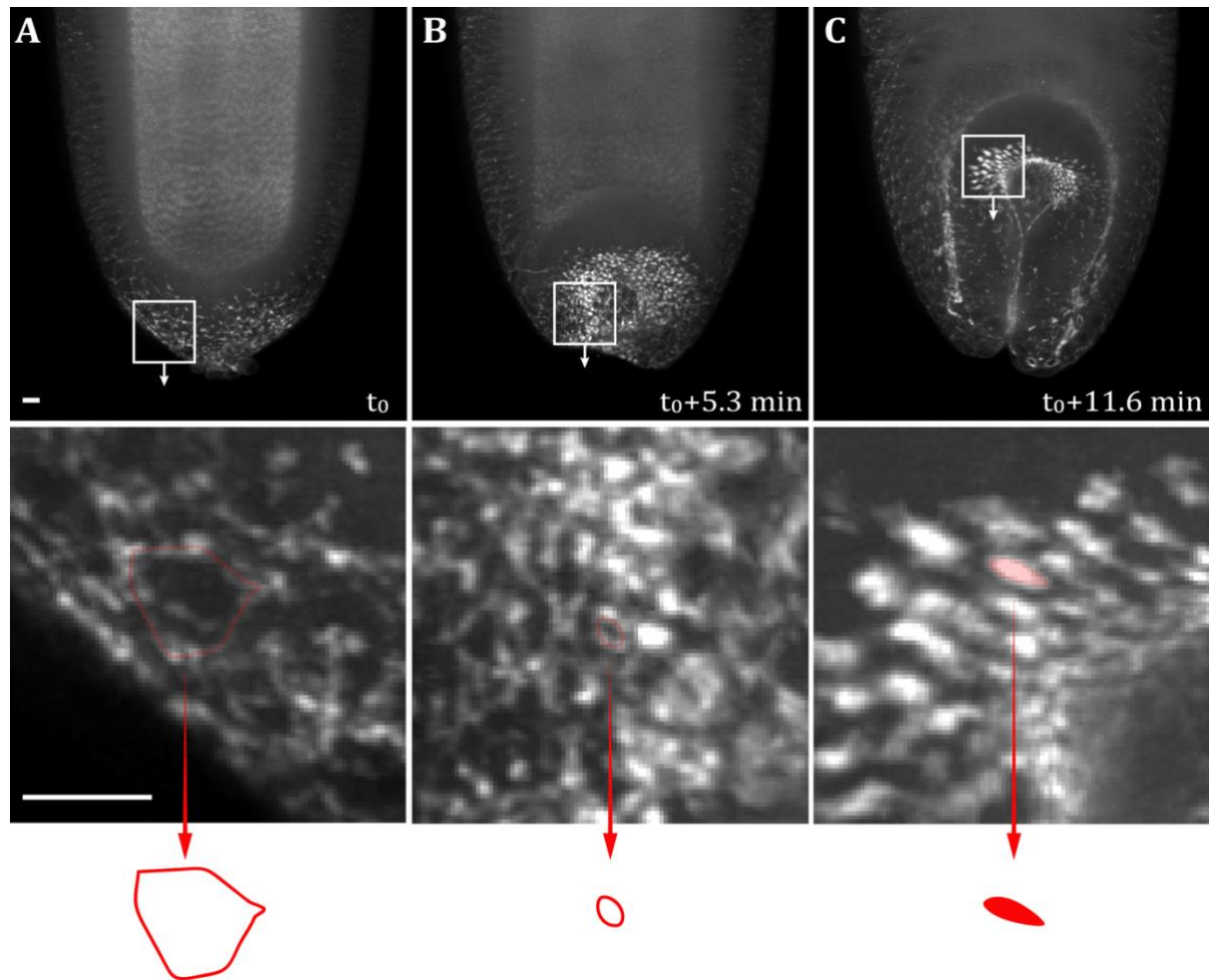


Fig. S7. Imaging of subcellular MyoII dynamics during posterior midgut invagination. Whole embryo volume imaging data were cropped to depict the dorsal posterior region of the embryo during posterior midgut invagination in a maximum intensity projection. **(A)** The initial phase of posterior midgut invagination is characterized by an apical accumulation of MyoII-GFP punctae that associate with the apical junctions of the cells in the posterior midgut primordium. **(B)** The MyoII-GFP punctae associated into ring-like structures within the apical areas of the cells in the primordium. **(C)** Further into posterior midgut invagination, additional MyoII-GFP aggregates form in the apical area of adjacent cells located in an anterior direction to the midgut primordium. Scale bars, 10 μ m.

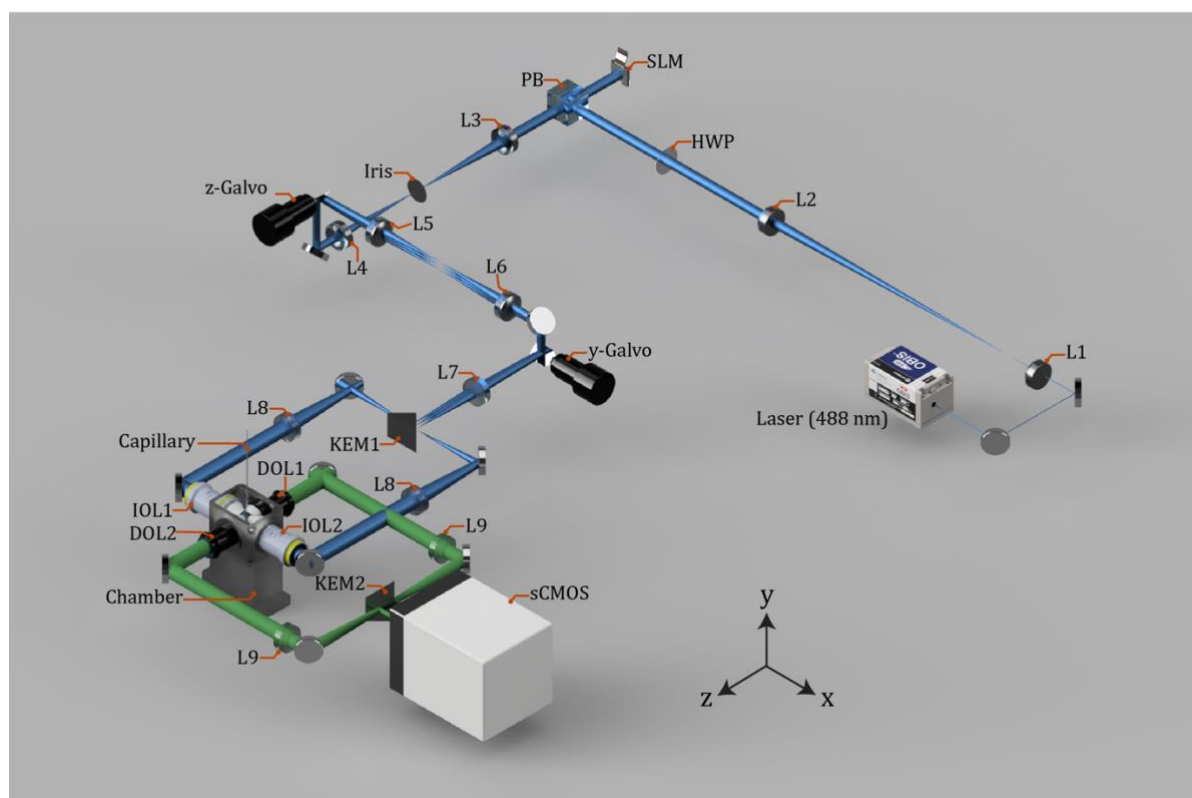


Fig. S8. Schematic of the MT-SPIM setup. The microscope includes two main optical arms: illumination and detection arm which are indicated with blue and green color. Within the illumination arm, a diode laser with 488nm wavelength operates as an illumination source to excite the green fluorescent protein (GFP) based sample. The optical beam's output diameter from the laser source is about 1 mm. It is not sufficient to interact with the spatial light modulator (SLM) with a diameter of around 12 mm. Hence, the optical beam is expanded to 12 mm diameter with two lenses telescope configuration (L1: 25 mm, L2: 300 mm) to cover the SLM area for an effective beam shaping. The light reflected from the SLM is passed through a lens (L3: 75 mm), creating a Fourier diffraction pattern. A pinhole filters the unwanted diffraction pattern caused by the inherent pixelated SLM's structure. The filtered light is then collected by another lens (L4: 75 mm) after an Iris pinhole to conjugate the pattern projected by the SLM. The conjugated illumination light heats the serial of optical elements such as a z-Galvo mirror, pair of two lenses (L5: 75 mm and L6: 75 mm), a y-Galvo mirror, and a transformer lens (L7: 75 mm). The z-Galvo mirror is used to reposition the illumination light through the sample for volume imaging which is conjugated using the pair lenses to the place of the y-Galvo mirror to produce the light sheet. The primary light sheet is detectable in the focal length of the transformer lens that is parked in front of the y-galvo mirror. The primary light sheet is faced with a knife-edge mirror (KEM 1) to send the light sheet into the right and left arm of the illumination beam for two side illuminations. The primary light sheet is then collected with the assembly of a lens (L8: 150 mm) and an illumination objective lens (IOL1 or IOL2, 10x Nikon water immersion) to deliver the light sheet to a specific layer of the sample. In the optical detection arms, which are indicated with green color, the emitted light from the sample is detected by two objective lenses (DOI1 and DOL2, 20x Olympus) simultaneously. In the final step, to record the image, the DOLs collect the signals from the sample and send them to a single sCMOS camera (V2 Orca-flash, Hamamatsu) which is combined by two tube lenses (L9: Olympus, 200 mm) and a knife-edge mirror (KEM 2) for simultaneous Multiview imaging.

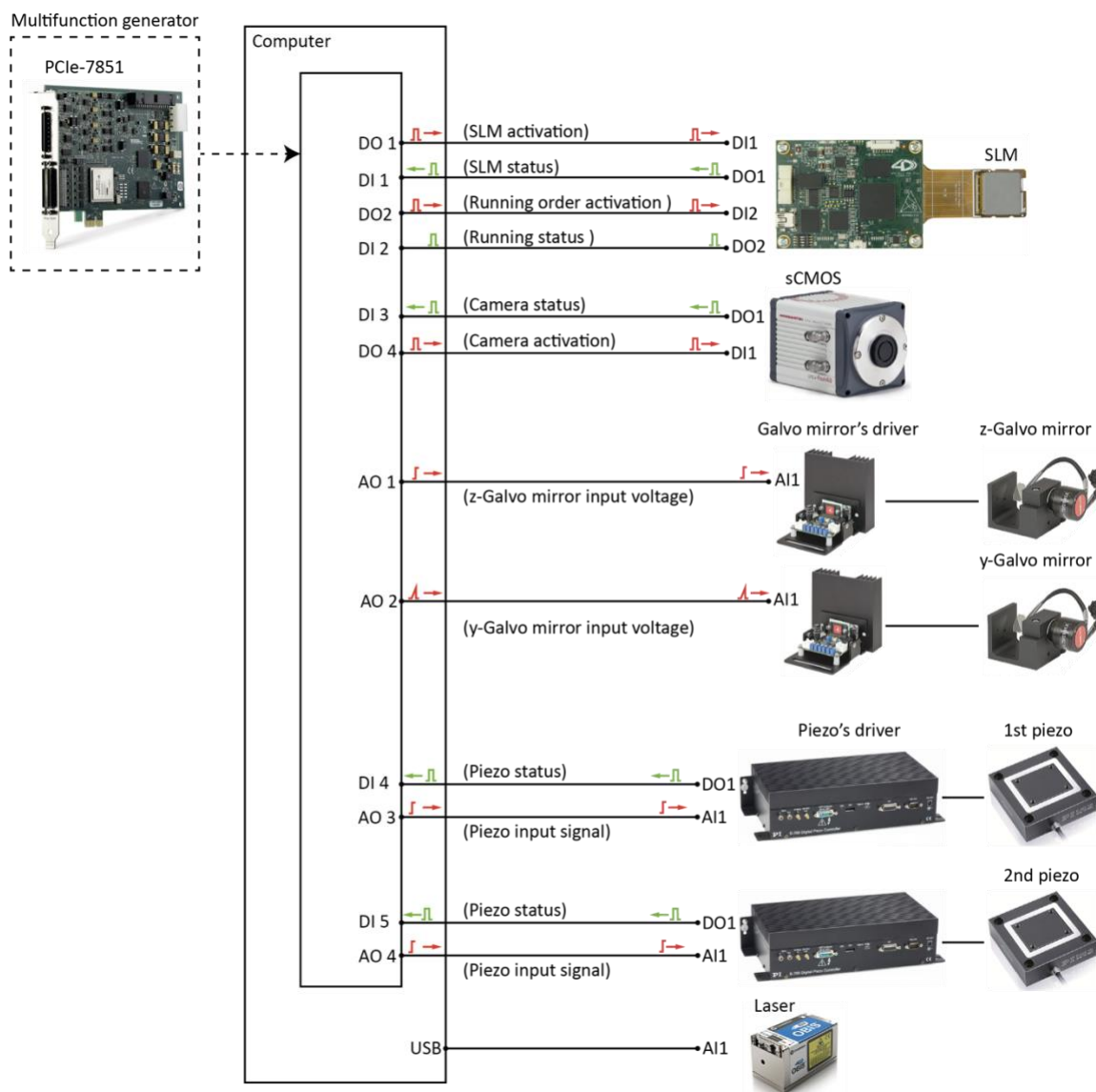


Fig. S9. Electronic structure of the MT-SPIM. The figure shows the architecture of the electronic connections between the components. A fast-programmable gate array (FPGA, PCIe-multifunction generator) is hosted for realtime signal controlling to have high-speed imaging. The electronic components are connected to the FPGA board with several digital and analog connections, which are indicated in the figure by digital input and digital output (DI and DO). All of the DI ports in the FPGA board operate parallel to monitor each component's status at the same time. The DO ports are also employed as emitter to send the command signal to each electronic part for a particular operation. In addition, the FPGA's analog output ports (AO) produce the analog electrical waveform for the component which are running based on the analogue signal such as scanning mirrors and piezoelectrics.

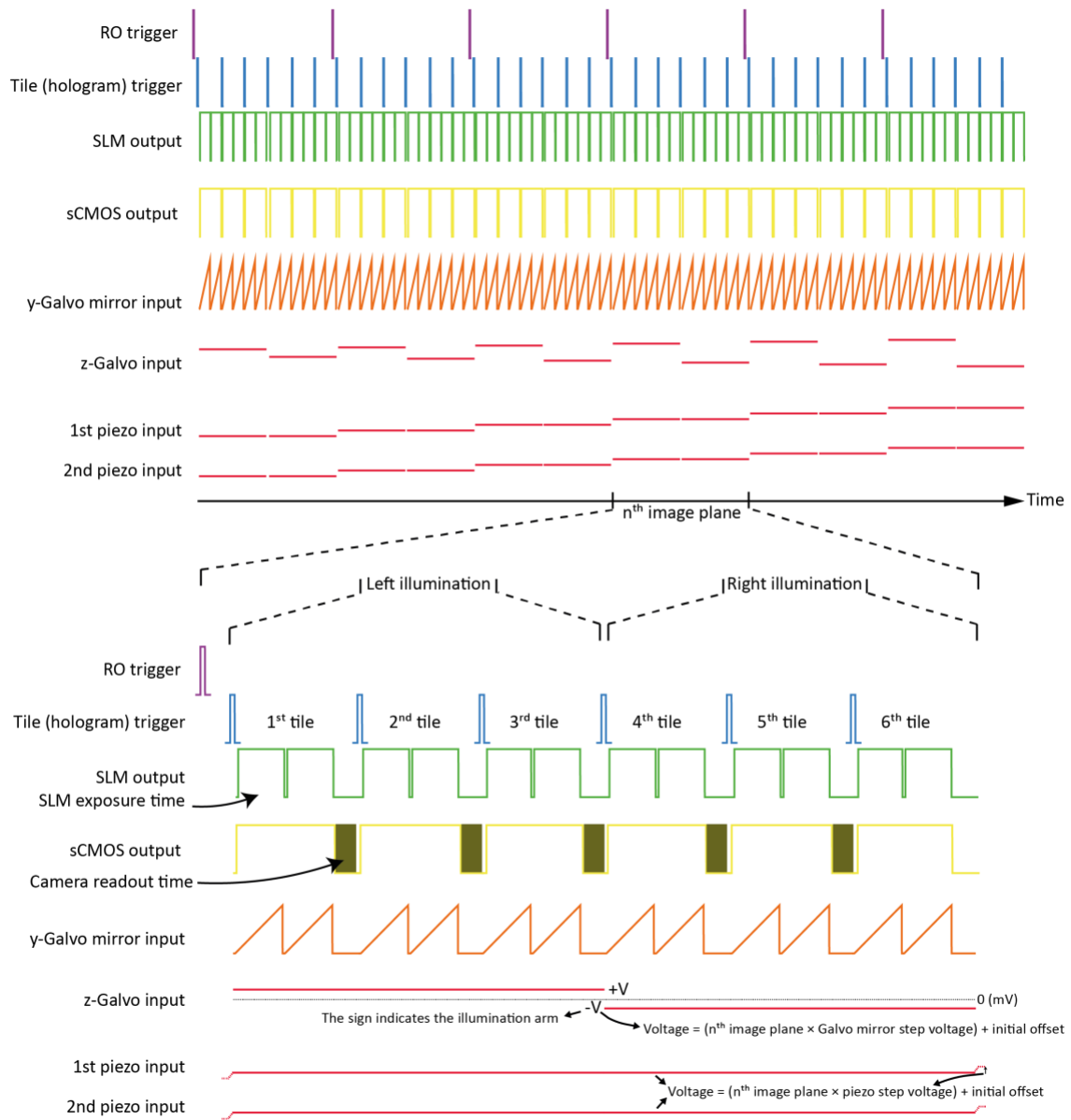
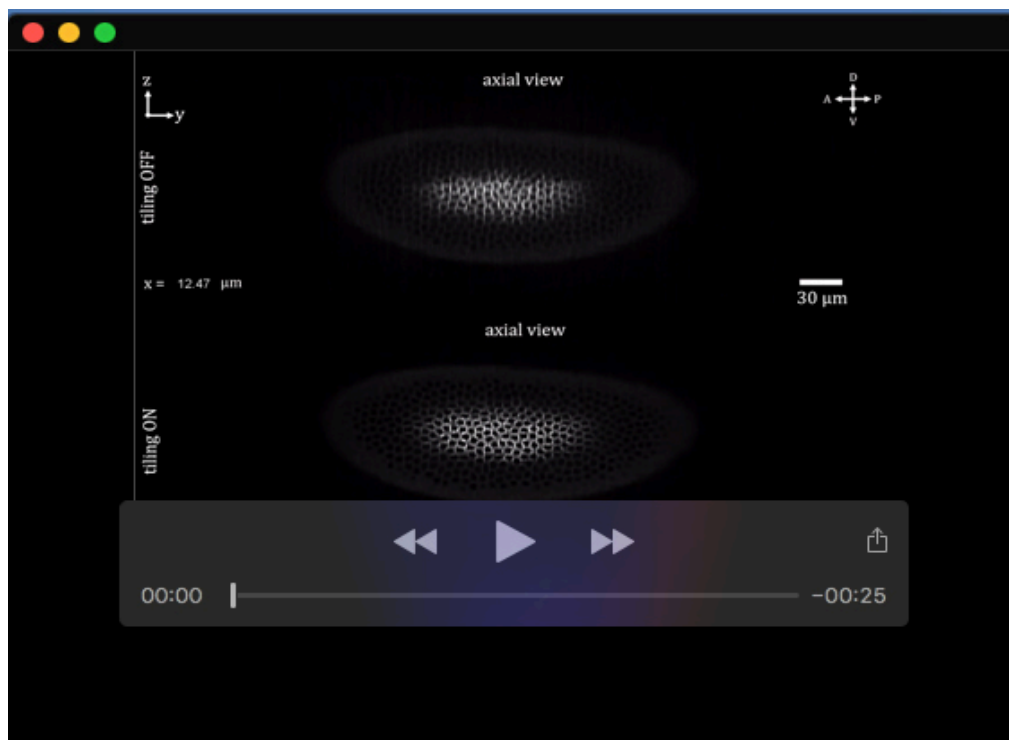
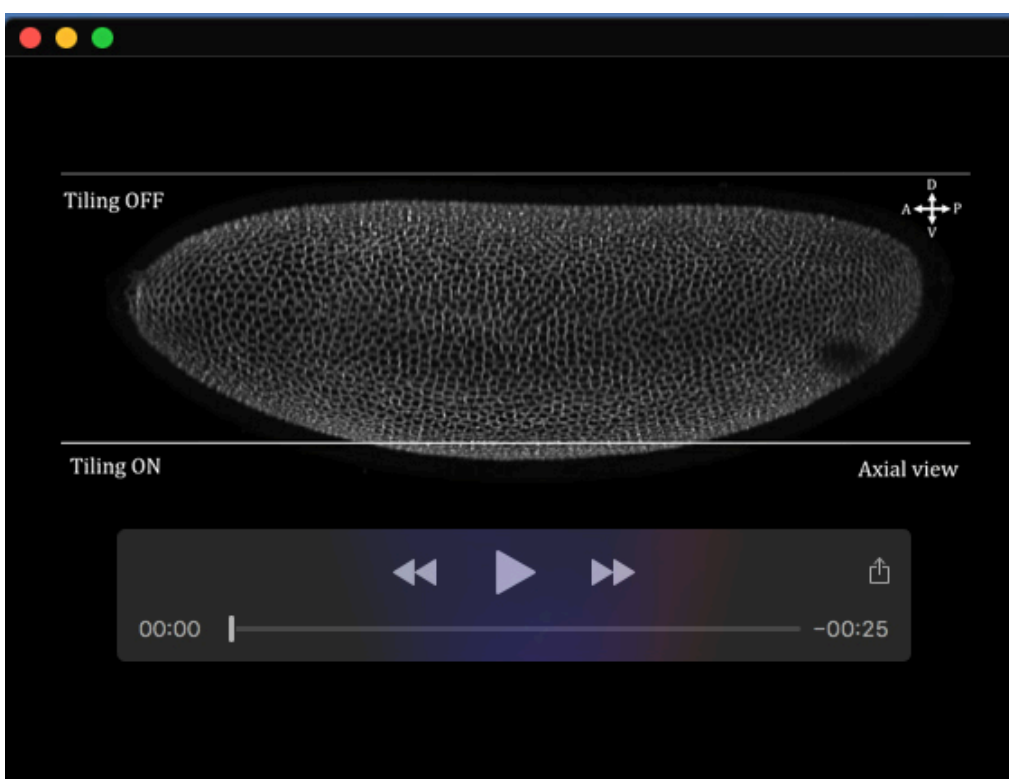


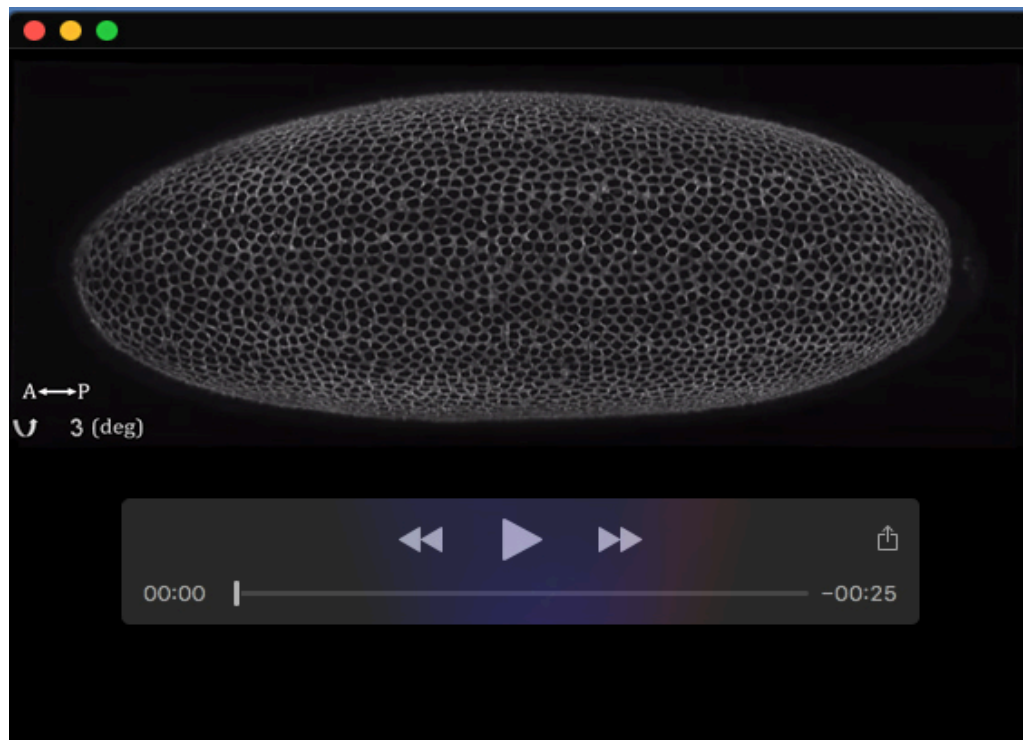
Fig. S10. The timing diagram of the MT-SPIM's electrical waveforms. All components operate based on predefined electrical waveforms. For each tiled light sheet the spatial light modulator (SLM) operates as a master clock, which is synchronized with camera exposure time. When the camera starts to collect the emitted light, the y-Galvo mirror is started to scan the illumination beam with a sawtooth wave to generate the light sheet. For the three tiled light sheets, the SLM, camera, and y-Galvo mirror operate simultaneously three times per illumination arm. All tiled light sheet illuminates a particular imaging plane which is tuned in the focus of the detection lens by the z-Galvo mirror with a constant voltage. After one complete illuminated arm, the three tiled light sheet switches to the second illumination arm by changing the z-Galvo mirror's voltage by a negative sign. In addition, in the detection side, to keep the detection objective lenses in focus for all tiled light sheet, the voltage of the piezos is settled constant during the imaging of a single plane. After that, piezoes' voltage are changed smoothly with a predefined step voltage to move the detection objective lenses to the next plane for 3D imaging.



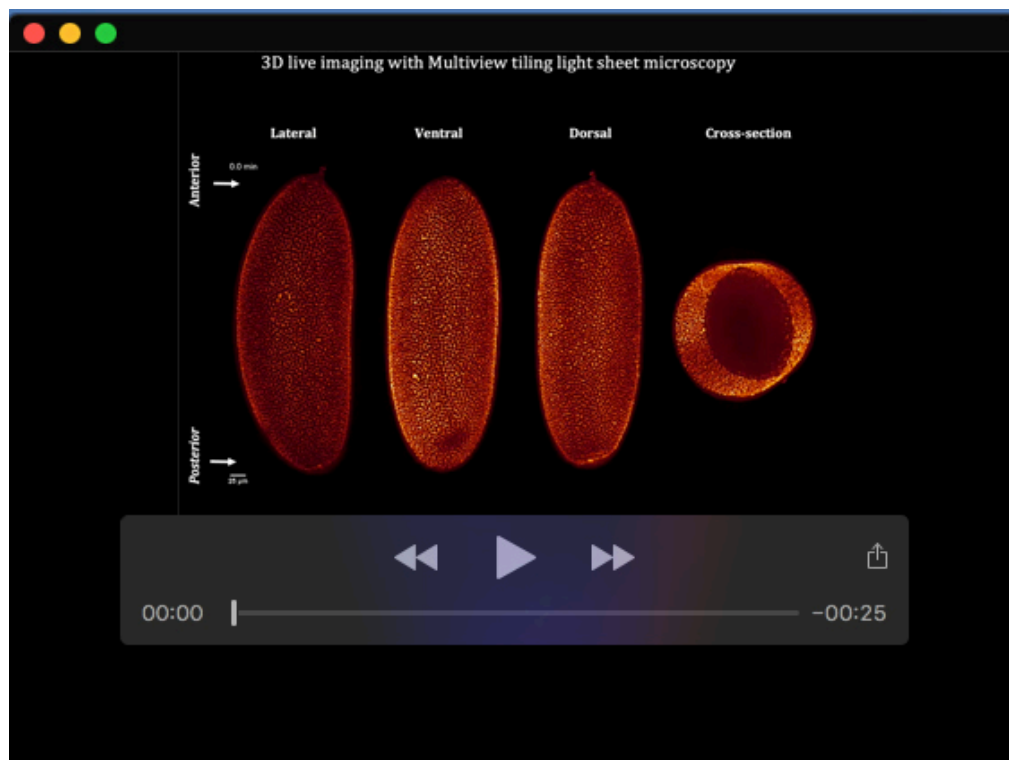
Movie 1. Comparison of the reconstructed axial images recorded by M-SPIM and MT-SPIM.



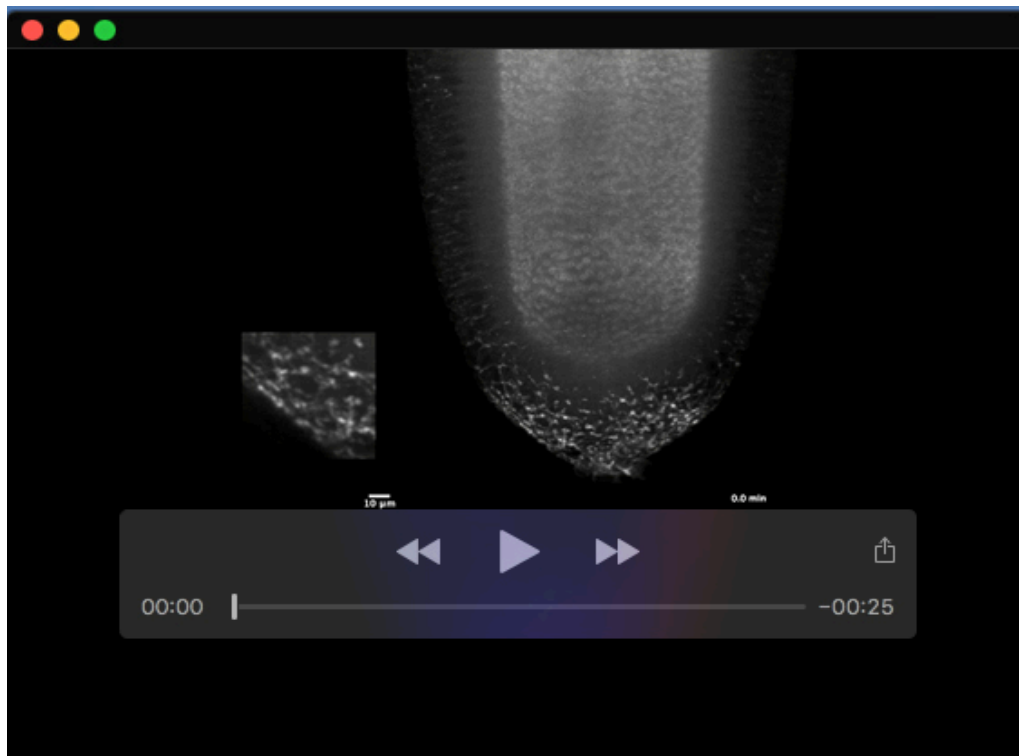
Movie 2. Maximum intensity projection of the reconstructed axial images recorded by MT-SPIM versus M-SPIM.



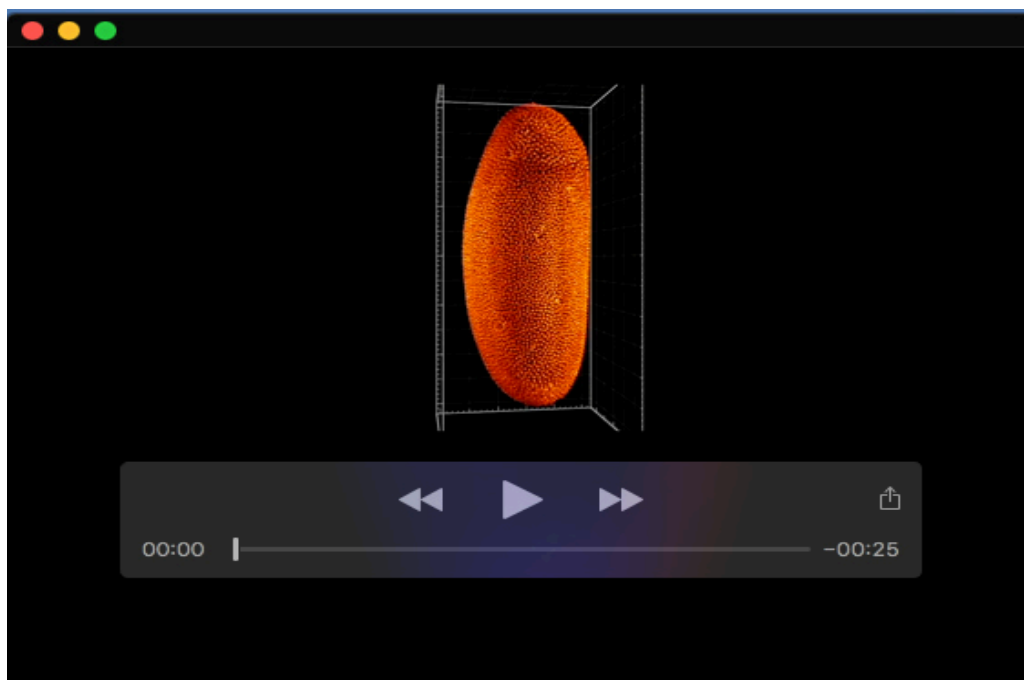
Movie 3. 3D rendering of a live *Drosophila* embryo image recorded by MT-SPIM at the start of the cellularization process.



Movie 4. 3D visualization of a live *Drosophila* embryo recorded by the MT-SPIM during cellularization and the early stages of gastrulation.



Movie 5. 3D rendering of a recorded live *Drosophila* embryo captured by the MT-SPIM during posterior midgut formation.



Movie 6. 3D rendering of a recorded live *Drosophila* embryo captured by the MT-SPIM during cellularization and early gastrulation compared to the M-SPIM.